Heat transfer evaluation of metal oxides based nano-PCMs for latent heat storage system application

Zakir Khan [a,b], Zulfiqar Ahmad Khan [a]*, Philip Sewell

[a] Bournemouth University, Department of Design & Engineering, NanoCorr, Energy and Modelling (NCEM) Research Group, Fern Barrow, Talbot Campus, Poole, Dorset BH12 5BB, UK.

[b] School of Mechanical & Manufacturing Engineering (SMME), National University of Sciences & Technology (NUST), Sector H-12, Islamabad – 44000, Pakistan.

Corresponding Author:

[a]* Bournemouth University, Department of Design & Engineering, NanoCorr, Energy and Modelling (NCEM) Research Group, Fern Barrow, Talbot Campus, Poole, Dorset BH12 5BB, UK.

E-mail: zkhan@bournemouth.ac.uk

Tel.: +44 1202-961645

Abstract

This article is focused on numerical analyses of commercially available metal-oxides as potential nano-additives for paraffin in thermal storage applications. Technical and economic prospects of metal-oxides based nano-PCMs are evaluated to help formulate selection criterion for nano-additives to achieve optimum thermal performance at acceptable cost. Numerical model based on enthalpy-porosity technique is developed which incorporates natural convection and transient variations in thermo-physical properties of nano-PCM. Numerical model is simulated for charging and discharging cycles of nano-PCMs in shell and tube heat exchanger at controlled temperatures. Transient simulations help in analysing heat transfer categorisation and isotherms distributions, solid–liquid interfaces propagations, charging and discharging rates, and overall thermal enthalpy. Inclusion of nano-particles increase the effective thermal conductivity and surface area for heat transfer, which results in enhanced charging and discharging rates. The conductive heat transfer, peak heat flux, charging and discharging rates are significantly enhanced by increasing volume concentration of nano-particles. The percentage enhancement in charging rates of SiO_2 based nano-PCM samples with 1% and 5% are 29.45% and 41.04%, respectively. Likewise, the discharging rates are improved by 21.09% and 30.08%, respectively. However, an increase in volume concentration reduces natural convection and overall thermal enthalpy, and increases total cost of nano-PCM. For instance, the percentage reductions in total enthalpy of CuO based nano-PCM samples with 1% and 5% volume concentrations are 8.01% and 32.14%, respectively. Likewise, the total costs are increased from 14.26 €/kg for base paraffin to 70.89 – 309.33 €/kg, respectively. Hence, the significance and originality of this research lies within evaluation and identification of preferable metal-oxides with higher potential for improving thermal performance at reasonable cost. This article will help bring significant impact to large-scale utilisation of low-carbon and clean energy technology in domestic and commercial applications.

Keywords

Thermal energy storage (TES); Latent heat storage (LHS); Phase change material (PCM); Nano-particles; Melting and solidification; Shell and tube heat exchanger

Nomenclature

C	mushy zone constant	ρ	density (kg/m^3)
C_p	specific heat capacity (kJ/kg.K)	μ	dynamic viscosity (kg/m.s)
d	diameter (m)	Φ_{VC}	volume concentration of nano-particles
f	liquid fraction of nano-PCM	Subscripts	
$\vec{g}$	gravitational acceleration (m/s^2)	i	initial
H	total enthalpy (kJ)	l	liquefied phase
k	thermal conductivity (W/m.K)	s	solidified phase
k_B	Boltzmann constant	pc	phase change
L	latent heat capacity (kJ/kg)	np	nano-particles
M_W	molecular weight	pcm	base paraffin
N_A	Avogadro number	$npcm$	nano-PCM
p	pressure (N/m^2)	ref	reference
q	heat source term (W/m^3)	Acronyms	
T	temperature (^{o}C)	Nu	Nusselt number
t	time (s)	Pr	Prandtl number
$\vec{V}$	velocity (m/s)	Ra	Rayleigh number
V	volume (m^3)	HTF	heat transfer fluid
w	weight of nano-particles (g)	LHS	latent heat storage
Greek		PCM	phase change material
α	small constant value	TES	thermal energy storage
β	thermal expansion coefficient (1/^{o}C)		

1. Introduction

The global socio-economic developments are associated with higher demands of primary energy supply. Since the industrial revolution, the ever increasing worldwide demands for primary energy supply have been escalated by 150%. Fossil fuels have remained the main sources to provide primary energy supply (about 80%) at the cost of energy security due to depleting natural resources and climate change due to emission of hazardous gases [1, 2]. To alleviate climate change and energy security challenges, the provision and development of effective and reliable technologies for renewable energy sources are vitally important. However, the intermittent and unpredictable nature of renewable energy sources are detrimental to wide-spread implementations. Thermal energy storage (TES) systems are determined as crucial technology to eradicate the energy supply and demand imbalance. Latent heat storage (LHS) utilises phase change materials (PCM) to capture and liberate thermal energy during phase transitions between solid–liquid at almost isothermal conditions. PCMs are available at broad range of phase transition temperatures with higher thermal storage capacity, lower vapour pressure and insignificant environmental hazards [3-5]. Despite being considered a promising approach, the wide-spread implementation of LHS systems are hindered by weaker charging and discharging rates caused by low thermal conductivity of PCMs (0.1–0.7 W/m.K). Hence, to minimise the impact of low thermal conductivity, several performance enhancement techniques have been recently devised and implemented such as: geometrical orientation of heat exchanger and inclusion of extended surfaces, inclusion of thermal conductive nano-additives and micro or nano encapsulations [6-9].

In case of geometrical configurations, the shell and tube heat exchanger coupled with extended surfaces are preferred due to their strengths in heat transfer, design simplicity and easier integration to applications. Rathod and Banerjee [10] reported that both charging and discharging rates of stearic acid in vertical shell and tube, with and without three longitudinal fins, were increased by 24.52% and 43.6%, respectively. Likewise, the inclusion of extended surfaces significantly increase thermal penetration in PCM. Lohrasbi et al. [11] noticed that the addition of longitudinal, circular and v-shaped fins improved the charging rates in vertical shell and tube by 3.26, 3.55 and 4.28 times as compared to no-fins configurations. Rabienataj Darzi et al. [12] concluded that both charging and discharging rates of n-eicosane were influenced by increasing number of longitudinal fins in shell and tube. It was observed from numerical simulation that as compared to no-fins, the charging and discharging times were reduced by 39–82% and 28–85% by increasing longitudinal fins from 4–20. Moreover, a novel geometrical configuration of shell and tube with multiple passes and longitudinal fins for large-scale applications was proposed in [13]. It was noticed that the optimised design under increasing inlet temperature from 50–70 ^{o}C significantly improved the phase transition rate and total enthalpy by 68.8% and 18.06%, respectively. Later on, the proposed novel design was experimented for series of charging and discharging cycles with connection to solar collector [14-16]. It was reported that the proposed design was capable of charging 14.35 MJ in 3 h and discharging 13.63 MJ in 1.5 h. Also, the mean charging and discharging powers were augmented by 69.71% and 36.05% with increasing temperature gradient.

Despite the excellent thermal enhancement, the extended surfaces significantly increase the overall weight of LHS system. Hence, the inclusion of nano-additives to improve the effective thermal conductivity is another promising approach with comparatively slighter increase in

overall weight. Nano-additives are classified into two main groups: a) carbon allotropes and b) metals or metal-oxides, nitrides and carbides [17].

Xia et al. [18] conducted experimental investigations on expanded graphite (EG) based PCM composite in heat recovery condenser. In case of optimum mass ratio of 10:1, the charging and discharging rates were increased by 81.7% and 55.3%, respectively. Likewise, Sharshir et al. [19] reported that the solar still productivity was increased by 73.8% with inclusion of graphite flakes based nano-PCM. Moreover, Yu et al. [20] reported that graphene nano-platelets have better thermal enhancement potential than carbon nano-tubes and carbon nano-fibres with relatively higher thermal conductivity and lower dynamic viscosity. Qian and Li [21] developed n-octadecane and diatomite decorated with carbon nano-particles based composite, which increased the thermal conductivity of composite from 0.24–0.73 W/m.K. Kant et al. [22] reported that inclusion of graphene nano-particles in capric acid, calcium chloride hexahydrate and n-octadecane increased the phase transition rates. However, the augmented dynamic viscosity of composites hindered the influence of natural convection. Moreover, Yuan et al. [23] reported significant reduction in latent heat capacity of graphene nano-platelets and expanded graphite based composite PCMs by 20.90% and 25.17%. Tang et al. [24] conducted experimental investigation on performance enhancement of MA/HDPE composite with Al_2O_3 and graphite nano-additives. It was reported that the effective thermal conductivity was significantly enhanced by 95.56% and 121.67%, respectively. Warzoha and Fleischer [25] experimentally investigated the thermal enhancement in base paraffin with inclusion of graphene, carbon nano-tubes, Al and TiO_2 nano-particles. It was reported that the total charging and discharging time for paraffin composites were reduced by 29.82%, 27.19%, 16.67% and 12.28%, respectively. Moreover, the thermal energy release was boosted by 11% for graphene based composite, whereas reductions in the range of 15–17% were noticed for other nano-additives. Alizadeh et al. [26] informed through numerical investigations that the solidification rates for TiO_2–Cu based composites were influenced by shape factors of nano-particles. Hexahedron, platelets and lamina nano-particles based composites were studied. It was noticed that due to relatively higher shape factor, the solidification rate for lamina nano-particles were higher as compared to hexahedron and platelets. However, the total thermal energy was inversely related to shape factor. Hosseinzadeh et al. [27] reported that the solidification rates for Al_2O_3–Go based composites with volume concentration of 2.5% and 5% were 1.74 and 2.69 times higher as compared to no nano-additives case. Likewise, as reported in [28], the charging/discharging rates and overall thermal enthalpy capture/release of base paraffin in shell and tube were significantly augmented with inclusion of Al_2O_3, AlN and graphene nano-additives. It was noticed that with inclusion of 1 vol% of nano-particles, the charging rates were augmented by 28.01%, 36.47% and 44.57%, and discharging rate by 14.63%, 34.95% and 41.46%, respectively. Owolabi et al. [29] reported an increase in effective thermal conductivity of paraffin from 0.25 W/m.K to 0.29, 0.33, 0.35 and 0.54 W/m.K for Al, Cu, Zn and Fe based nano-PCM composites with 1.5 wt%. However, Lin and Al-Kayiem [30] reported that with an increase in concentration from 0.5–2 wt% for Cu based paraffin composites, the latent heat was reduced from 184.2 kJ/kg for base paraffin to 172.2–157.3 kJ/kg, respectively.

Said and Hassan [31] examined the power saving potential of air-conditioning unit coupled with nano-PCM based heat exchanger instead of conventional condenser unit. It was reported that the power saving was increased from 7.18% for pure paraffin to 7.28%, 7.35%

and 7.41% for Al_2O_3, CuO and Cu based nano-PCM samples with 5 vol%. Harikrishnan et al. [32] reported that thermal conductivity of LA/SA was significantly increased by 34.85%, 46.97% and 62.12% with inclusion of TiO_2, ZnO and CuO with 1 wt%. Thus, the melting rates were improved by 11.39%, 15.54% and 21.24%, and solidification rates by 5.56%, 13.89% and 19.84%, respectively. Babapoor et al. [33-35] examined the impact of Al_2O_3, Fe_2O_3, SiO_2, and ZnO nano-additives with different concentrations on thermal performance of paraffin, polyethylene glycol and eutectics fatty acids. For all cases, thermal conductivity was significantly enhanced and noticeable reduction in latent heat was reported. Al_2O_3 and SiO_2 were suggested as preferable nano-additives due to their reasonable reduction in latent heat. It was also noticed that nano-additives response to thermal enhancement is dependent on base materials. However, the higher potentials of thermal performance enhancement by inclusion of nano-additives to base materials are usually undermined by weaker dispersion and long-term suspension stability [36, 37]. Therefore, the agglomeration and sedimentation problems in nano-PCMs should be minimised by ultrasonication and inclusion of compatible surfactants [38, 39]. Moreover, the higher volume concentration of nano-additives aggravate the agglomeration and sedimentation issues [40, 41], which results in weaker thermo-physical stability, uniform thermal distribution and natural convection. Hence, it is imperative to identify the optimum volume concentration and to investigate the thermo-physical stability by conducting accelerated charging and discharging cycles [42, 43].

In recent years, a significant body literature is published on synthesis and characterisations of various metal oxides, nitrides and carbides based nano-PCMs with different concentrations to achieve thermal enhancement [44-47]. However, the majority of literature is focused on synthesis of nano-PCMs and there is lack of investigations on optimum concentration for nano-additives and respective thermo-physical analyses of nano-PCMs in actual heat exchanger. Literature also lacks comparative and all-inclusive thermal analyses of commercially available metal-oxides based nano-PCMs with varied volume concentrations in heat exchanger. Moreover, the literature lacks to provide a detailed insight into economic assessment of metal-oxides enhanced nano-PCMs and a holistic selection criterion for nano-additives to achieve optimum thermal enhancement at reasonable price.

This article aims to conduct a comprehensive numerical analyses on fourteen commercial metal-oxides based nano-PCM samples with three volume concentrations to evaluate their thermo-economic performance in shell and tube heat exchanger, which are neither considered in [13-15, 28] nor reported in previous literature. Numerical model for nano-PCM include the effects of thermo-physical properties of base material and metal-oxides, nano-particles size and volume concentrations, and operating temperature. Transient numerical simulations are conducted for both charging and discharging cycles for all nano-PCM samples. Thermal performance evaluations include charging/discharging rates, total enthalpy capture/release, heat transfer characterisation and natural convection assessment, temperature/enthalpy distribution and solid-liquid interfaces propagation in shell container. Numerical simulation results are validated with experimental results for both charging and discharging cycles. Furthermore, the economic valuation of nano-PCM samples help distinguish appropriate metal-oxides for wide-ranging domestic and commercial applications.

2. Numerical Model

2.1. Physical model and computational domain

The schematic of physical model and cross-sectional geometrical dimensions of shell and tube heat exchanger and nano-PCM based LHS unit is illustrated in **Fig. 1**. The horizontal shell and tube heat exchanger is made of acrylic plastic shell container and seven stainless steel tubes. The length, inner and outer diameter of shell container are 185 mm, 50 mm and 60 mm, respectively. Exterior boundary of shell container is insulated with glass wool. Similarly, the inner and outer diameter of tubes are 4 mm and 6 mm, respectively. Water is utilised as heat transfer fluid (HTF), which is regulated to flow through tubes and transfer thermal energy with nano-PCM in shell container. Paraffin (RT44HC) is considered as base material and metal-oxides as nano-additives. **Table 1** provides the thermal and physical characteristics of base paraffin. The materials specifications, thermal and physical properties and cost of commercially available metal-oxides nano–particles are listed in **Table 2**. For each metal–oxide, three nano-PCM samples are investigated with volume concentration of 1%, 3% and 5%. Hence, this article provide holistic charging and discharging cycles' performance of 42 nano-PCM samples.

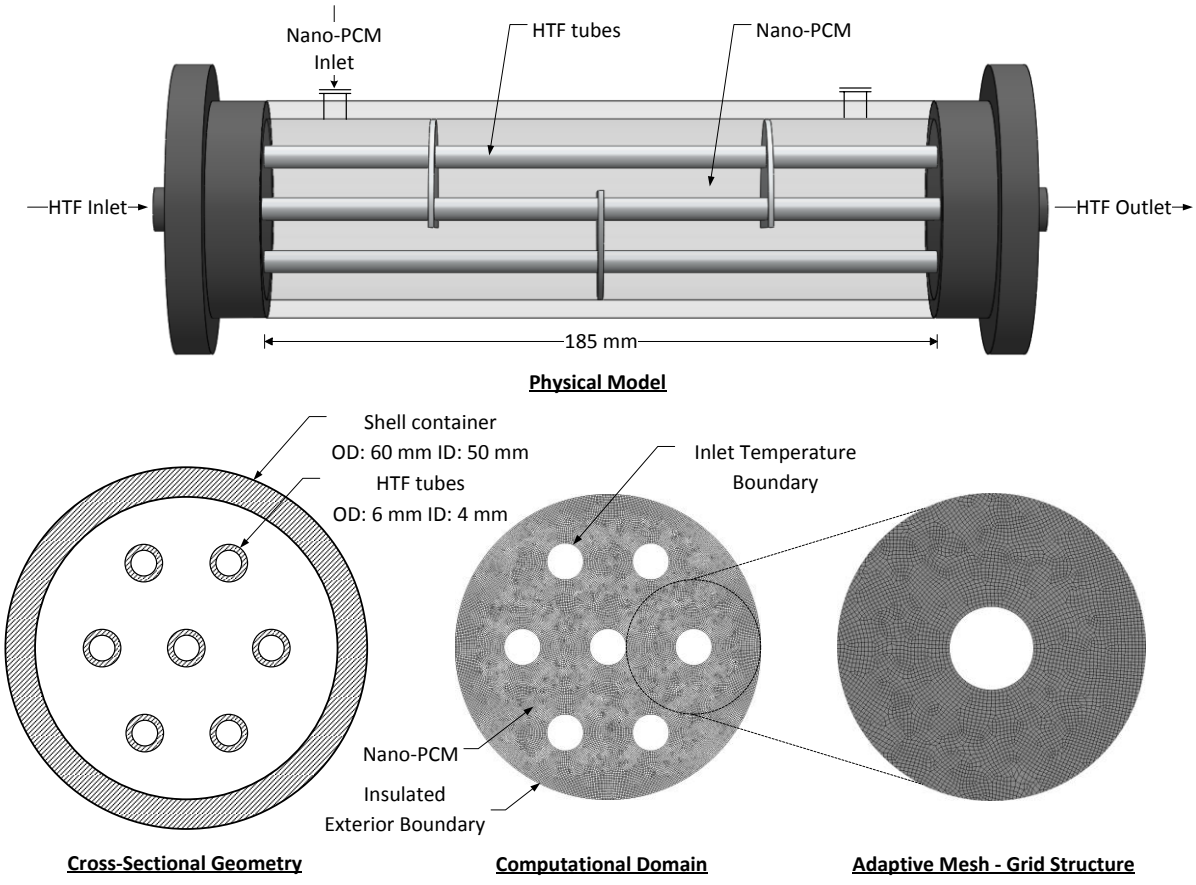

Fig. 1 Schematic of physical model, cross-sectional geometry, computational domain and grid structure of shell and tube HX with nano-PCM based LHS unit.

Table 1
Thermal and physical specifications of paraffin (RT44HC) [48]

Phase change temperature (^oC)	41-44	
Latent heat of fusion (kJ/kg)	255	
Density (kg/m^3)	800 (s)	700 (l)
Thermal conductivity (W/m.K)	0.2 (s)	0.2 (l)
Specific heat capacity (kJ/kg.K)	2 (s)	2 (l)
Volumetric heat capacity (kJ/m^3.K)	1600 (s)	1400 (l)

Table 2
Thermal and physical properties of nano-particles along with suppliers and prices [49, 50]

Nano-particle Materials	Density (kg/m^3)	Thermal Conductivity (W/m.K)	Specific Heat Capacity (kJ/kg.K)	Volumetric Heat Capacity (kJ/m^3.K)	Suppliers and Prices			
					IoLiTec nanomaterials	weight (g)	Sigma - Aldrich	weight (g)
Aluminum oxide (Al_2O_3), 20 nm	3980	38.493	0.778	3096.44	€ 49.00	100	£61.50	50
Cerium (IV) Oxide (CeO_2), 15-30 nm	6100	11.715	0.352	2147.20	-	-	£80.20	25
Cobalt Oxide (CoO), 30 nm	6460	10.042	0.703	4541.38	€ 49.00	100	£47.70	25
Copper Oxide (CuO), 40-80 nm	6500	17.991	0.536	3484.00	€ 69.00	100	£62.00	25
Gadolinium Oxide (Gd_2O_3), 20-80 nm	7640	10.042	0.290	2215.60	-	-	£184.50	10
Iron Oxide (Fe_2O_3), 20-40 nm	5240	12.552	0.628	3290.72	€ 89.00	100	£86.10	25
Magnesium Oxide (MgO), 35 nm	3580	61.923	0.921	3297.18	€ 49.00	100	£290.00	25
Nickel Oxide (NiO), 20 nm	6400	12.970	0.603	3859.20	€ 89.00	100	£37.00	25
Silicon Oxide (SiO_2), 10-20 nm	2650	11.715	0.753	1995.45	€ 49.00	100	£74.80	50
Strontium Titanate ($SrO.TiO_3$), 100 nm	5110	05.858	0.536	2738.96	€ 45.00	100	£106.50	50
Tin Oxide (SnO_2), 100 nm	5560	31.380	0.343	1907.08	€ 79.00	100	£176.50	25
Titanium Oxide (TiO_2), 100 nm	4250	08.954	0.686	2915.50	€ 59.00	100	£55.90	25
Yttrium Oxide (Y_2O_3), 30-50 nm	5000	14.226	0.448	2240.00	€ 59.00	100	£110.50	25
Zinc Oxide (ZnO), 100 nm	5630	27.196	0.494	2781.22	€ 59.00	50	£63.00	50

2.2. Governing equations

To conduct numerical investigations on charging and discharging cycles of nano-PCM samples in proposed computational domain, the following assumptions are considered to reduce computational time and complexity:

(i) Liquid phase of nano-PCM samples and their movement in shell container are laminar, incompressible and Newtonian in nature.
(ii) Volumetric expansion or contraction of samples associated with phase transition in shell container are neglected.
(iii) Due to low thermal conductivity of shell container material and exterior boundary insulation, the shell material is not considered in computational domain and adiabatic conditions are applied to outer boundary to avoid heat transfer with surrounding.
(iv) Due to relatively higher thermal conductivity of tubes material, the thickness of tubes are neglected and temperature variations of HTF are also ignored.
(v) Boussinesq approximation is implemented to compute for variation in density and respective buoyancy driven natural convection.

The governing equations for evaluating charging and discharging rate, thermal energy capture and retrieval, liquid phase propagation and temperature distribution in shell

container, transient heat flux and dimensionless numbers for nano-PCM samples are given below [51-53]:

Mass conservation:

$$\frac{\partial \rho_{npcm}}{\partial t} + \nabla.\left(\rho_{npcm}\vec{V}\right) = 0 \tag{1}$$

Momentum conservation:

$$\frac{\partial\left(\rho_{npcm}\vec{V}\right)}{\partial t} + \rho_{npcm}\vec{V}.\left(\nabla.\vec{V}\right) = -\nabla p_{npcm} + \mu_{npcm}\nabla^2.\vec{V} + \rho_{npcm}\beta_{npcm}\vec{g}(T_{npcm} - T_{pc}) + \frac{C(1-f)^2}{(f^3+\alpha)}\vec{V} \tag{2}$$

Energy conservation:

$$\frac{\partial\left(\rho_{npcm}H_{npcm}\right)}{\partial t} + \nabla.\left(\rho_{npcm}H_{npcm}.\vec{V}\right) = k_{npcm}\nabla^2.T_{npcm} + q \tag{3}$$

In momentum conservation Eq. (2), the second term on left hand side represent the convective term. Similarly, the terms on right hand side symbolise the pressure gradient, viscous diffusion, buoyant forces and momentum source terms [53]. Boussinesq approximation [54] is implemented to compute the buoyancy driven natural convection. The buoyant forces regulate upward movement of higher temperature and lower density nano-PCM molecules. Natural convection has significant influence on melting process of nano-PCM. Moreover, enthalpy–porosity method is considered for modelling solid–liquid phase transitions. Darcy law for porous medium [55] is implemented for momentum source term, which evaluates the porosity in mushy zone. C represents the morphological constant to control damping effects in mushy zone due to variations in velocity with phase transitions. In current study, the numerical results are in good agreement with experimental results for $C = 10^6$. Likewise, f represents liquid fraction, which ranges between 0–1 as temperature of nano-PCM varies between solidus and liquidus phase, as follow [51, 52]:

$$f = \begin{cases} 0 & T_{npcm} < T_s \\ \dfrac{T_{npcm} - T_s}{T_l - T_s} & T_s \le T_{npcm} \le T_l \\ 1 & T_{npcm} > T_l \end{cases} \tag{4}$$

In energy conservation Eq. (3), the second term on left hand side denote the thermal convection due to rotational and transitional motions of nano-PCM. Likewise, the right hand side represent the heat conduction and volumetric heat source terms. H_{npcm} represents the total enthalpy of nano-PCM which includes both sensible and latent portions, as given below [51, 52]:

$$H_{npcm} = h_{ref} + \int_{T_{ref}}^{T_{npcm}} C_p dT + fL \tag{5}$$

where h_{ref} and L represent reference enthalpy (at $T_{ref} = T_i$) and latent heat capacity of nano-PCM, respectively.

2.3. Nano-PCM thermo-physical properties relations

Thermo-physical properties of base material (RT44HC) and metal-oxides nano–particles are listed in Table 1 and Table 2, respectively. Inclusion of metal-oxides nano–particles have presented significant influence on thermo–physical properties of nano-PCM [24, 32, 56, 57]. Therefore, the relations for mixture of two components are implemented to estimate the corresponding thermo-physical properties of nano-PCM [28, 37]:

$$\rho_{npcm} = (1 - \Phi_{VC})\rho_{pcm} + \Phi_{VC}\rho_{np} \tag{6}$$

$$C_{p,npcm} = \frac{(1 - \Phi_{VC})\rho_{pcm}C_{p,pcm} + \Phi_{VC}\rho_{np}C_{p,np}}{\rho_{npcm}} \tag{7}$$

$$L_{npcm} = \frac{(1 - \Phi_{VC})\rho_{pcm}L_{pcm}}{\rho_{npcm}} \tag{8}$$

$$\beta_{npcm} = \frac{(1 - \Phi_{VC})\rho_{pcm}\beta_{pcm} + \Phi_{VC}\rho_{np}\beta_{np}}{\rho_{npcm}} \tag{9}$$

where Φ_{VC} represents the volume concentration of metal-oxides nano–particles. Likewise, the dynamic viscosity of nano-PCM varies with volume concentration and material specifications of nano-particles. Hence, the transient modifications in effective dynamic viscosity of nano-PCM are estimated by semi-empirical model proposed by Corcione [58], as follow:

$$\mu_{npcm} = \frac{\mu_{pcm}}{1 - 34.87\left(d_{np}/d_{pcm}\right)^{-0.3}{\Phi_{VC}}^{1.03}} \tag{10}$$

where μ_{pcm} represents the dynamic viscosity of base paraffin and is determined as follow [59]:

$$\mu_{pcm} = 0.001exp\left(-4.25 + \frac{1790}{T_{pcm}}\right) \tag{11}$$

d_{pcm} shows the equivalent diameter of base paraffin and is calculated as follow [58]:

$$d_{pcm} = 0.1\left(\frac{6M_W}{\pi N_A \rho_{pcm,o}}\right)^{\frac{1}{3}} \tag{12}$$

where $\rho_{pcm,o}$ represents the density of base paraffin at $T_{pcm} = 20$ ℃.

Moreover, the transient variations in effective thermal conductivity of nano-PCM are approximated by employing the proposed model by Vajjha and Das [60], as follow:

$$k_{npcm} = \frac{k_{np} + 2k_{pcm} - 2\left(k_{pcm} - k_{np}\right)\Phi_{VC}}{k_{np} + 2k_{pcm} + \left(k_{pcm} - k_{np}\right)\Phi_{VC}}k_{pcm} + 5 \times 10^4\zeta\rho_{pcm}\Phi_{VC}C_{p,pcm}\sqrt{\frac{\kappa_B T_{npcm}}{\rho_{np}d_{np}}}f(T, \Phi_{VC}) \tag{13}$$

where the correction factor $f(T, \Phi_{VC})$ is defined as:

$$f(T, \Phi_{VC}) = (2.8217 \times 10^{-2}\Phi_{VC} + 3.917 \times 10^{-3})\left(\frac{T_{npcm}}{T_{ref}}\right) + (-3.0669 \times 10^{-2}\Phi_{VC} - 3.91123 \times 10^{-3}) \quad (14)$$

Vajjha and Das [60] model for evaluating the effective thermal conductivity of nano-PCM accounts for the effects of nano–particles size, volume concentration, operating temperature, thermo–physical properties of both base paraffin and nano-particles, and the effects of Brownian motion of nano-particles in liquid phase. Whereas, the earlier models proposed by Maxwell [61], Bruggeman [62], Hamilton and Crosser [63] and Xuan et al. [64] were significantly dependent on volume fractions of nano-additives. Therefore, the effective thermal conductivity values were either not influenced or were under/over predicted at varying operating temperatures. However, the implemented proposed model by Vajjha and Das [60] was validated with experimental thermal conductivity values for Al_2O_3, CuO and ZnO nano-additives enhanced composites, with average percentage deviations of 0.23%, 5.74% and 1.97%, respectively. Hence, Eq. (13) and Eq. (14) are utilised to calculate the effective thermal conductivity of all fourteen metal-oxides nano–particles listed in Table 2, with volume concentration of 1%, 3% and 5%. **Fig. 2** illustrates the transient variation in effective thermal conductivity of nano-PCM samples with respect to temperature. It is noticed that the effective thermal conductivity of nano-PCM samples are higher for metal-oxides with smaller density. For instance, due to relatively smaller density of SiO_2 nano–particles, the effective thermal conductivity of respective nano-PCM samples with all three volume concentrations are significantly higher as compared to other metal-oxides.

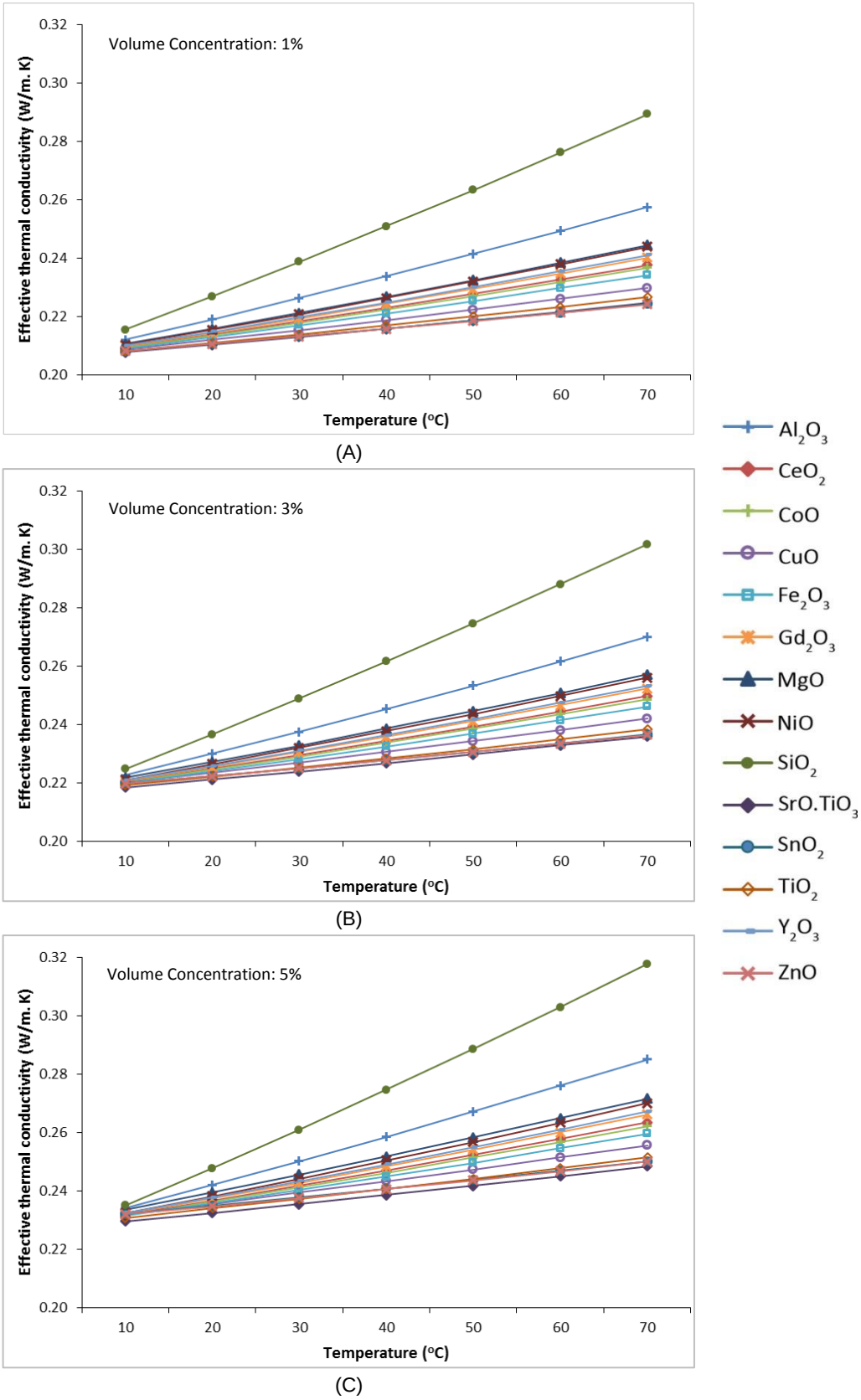

Fig. 2 Effective thermal conductivity of nano-PCMs with three different volume concentrations: (A) 1%, (B) 3% and (C) 5%.

2.4. Initial and boundary conditions

In case of charging cycles, the nano-PCM in shell container is set to initial temperature of 15 ^{o}C which confirms a complete initial solid phase. Moreover, the inlet temperature boundaries in computational domain, representing the HTF tubes, are given a constant temperature of 52 ^{o}C. Similarly, in case of discharging cycles, the initial temperature of nano-PCM are set to 52 ^{o}C to ensure complete liquid state and the inlet temperature boundaries are kept constant at 15 ^{o}C. The initial velocity $\vec{V}$ of nano-PCM in shell container is kept at zero in both charging and discharging cycles. The outer boundary of shell container in computational domain is set to adiabatic conditions.

2.5. Numerical simulation technique

Finite volume method is implemented to discretise the governing equations for complex flow nature of nano-PCM in computational domain [65]. Pressure–based solver is selected for solving the transient problem for charging and discharging cycles. Pressure–implicit with splitting of operators (PISO) scheme is preferred for solving transient pressure–velocity coupling in momentum conservation equation. Further, the spatial discretisation of pressure, momentum and energy conservation equations are conducted by pressure staggering option (PRESTO) and second order upwind algorithms. Absolute convergence criterion is adopted for residual monitoring of continuity, momentum, energy and $k-\varepsilon$ equations with residual values of 10^{-6}, respectively. Moreover, the first order implicit formulation for fixed time-stepping iterative advancement is selected to achieve stable solutions in both charging and discharging cycles.

2.6. Time step and grid independency tests

To ensure accuracy of simulation results, the time-step and grid resolution independency for computational domain are evaluated. Three time-steps of 0.1, 0.5 and 1 s are simulated for MgO – 1 vol% nano-PCM sample in computational domain, with fixed grid resolution of 27420, as presented in **Fig. 3 (A)**. The liquid fraction curves for all three time steps are almost identical throughout the charging cycle. Therefore, the time step of 0.1 s is chosen to secure higher accuracy. Similarly, three grid resolutions of 6930, 27420 and 78675 are examined with fixed time step of 0.1 s, as shown in **Fig. 3 (B)**. It can be noticed that the liquid fraction curves for grid resolution of 27420 and 78675 are matching. Therefore, to reduce computational time, the grid size of 27420 is chosen.

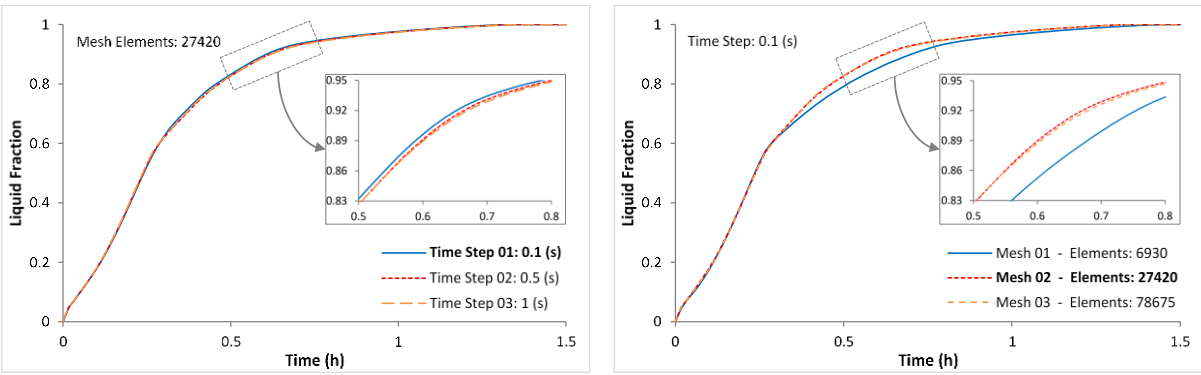

(A) (B)

Fig. 3 Time step and mesh size independency tests with 1% volume concentration of MgO based nano-PCMs: (A) liquid fraction of different time steps and (B) liquid fraction of different mesh sizes.

2.7. Experimental Validation

To validate numerical simulation results with experimental data, an experimental setup is designed which is comprised of shell and tube heat exchanger with identical geometry to the computational domain, preparation of nano-PCM sample through ultrasonic emulsification technique and experimental investigation of nano-PCM sample in heat exchanger, as presented in **Fig. 4** [28]. Calculated quantity of Al_2O_3 nano–particles is loaded in pre–melted base paraffin and a good suspension is achieved by magnetic stirring for 1 h with intensive ultrasonication for another 2 h for preparing nano-PCM sample. Further details related to ultrasonic emulsification of nano–particles in base paraffin and experimental tests of nano-PCM samples in heat exchanger can be found in [28]. Nano-PCM sample in heat exchanger is subjected to charging and discharging cycles at inlet temperatures of 52 ^{o}C and 15 ^{o}C, respectively. Two K–type thermocouples (K1 and K2) are installed at top and bottom position in shell container to register transient temperature response of nano-PCM sample during charging and discharging cycles, as shown in **Fig. 5**. It can be noticed that during charging cycles, the transient temperature curves for numerical and experimental tests are in good agreement, with mean absolute error of 1.31% (for K1) and 2.17% (for K2), respectively. During discharging cycles, the transient temperature curves represent excellent agreement within latent heat discharge region. However, the temperature drop during sensible heat discharge region is rapid for numerical simulation as compared to experimental tests. Due to which, the mean absolute error is slightly increased to 9.51% (for K1) and 8.67% (for K2) for discharging cycles. Despite that, the numerical model has demonstrated acceptable validation with experimental results.

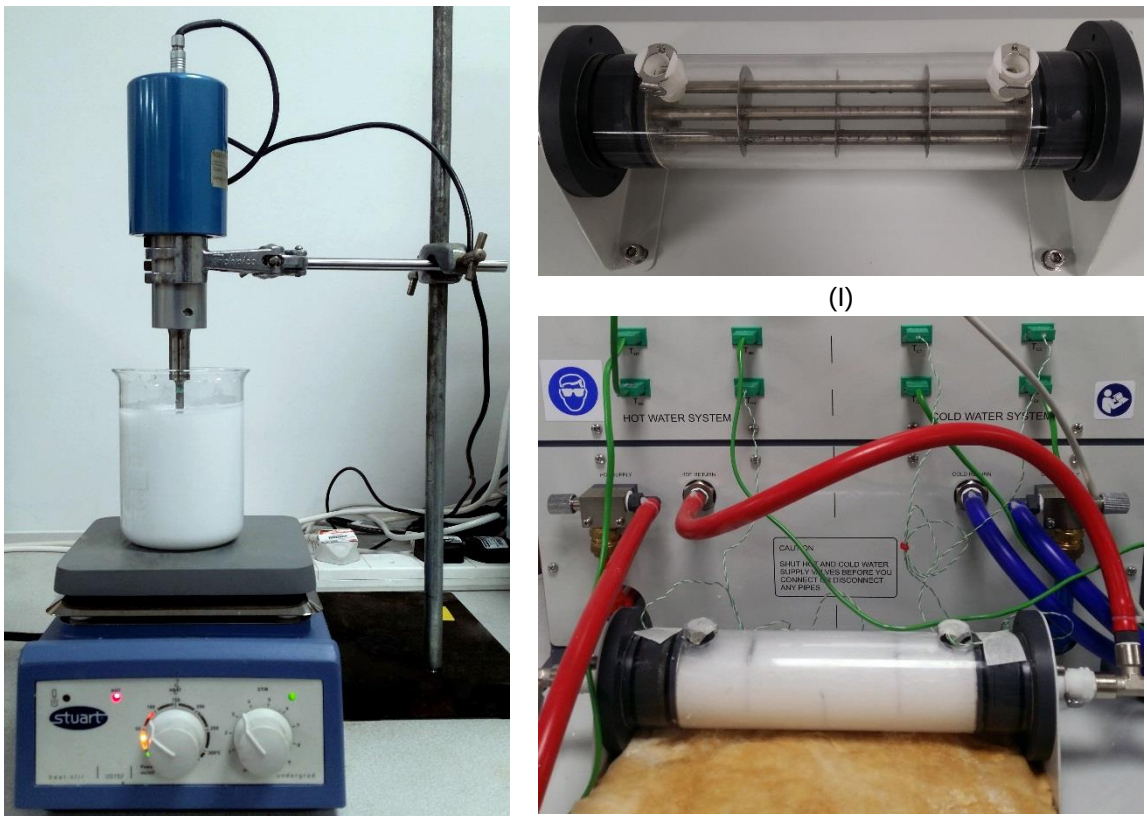

(I) (II) (III)

Fig. 4 Experimental steps involving formation of Al_2O_3 based nano-PCM sample and its charging in shell container: (I) shell and tube heat exchanger, (II) ultrasonic emulsification to develop nano-PCM sample and (III) filling the shell container with nano-PCM sample.

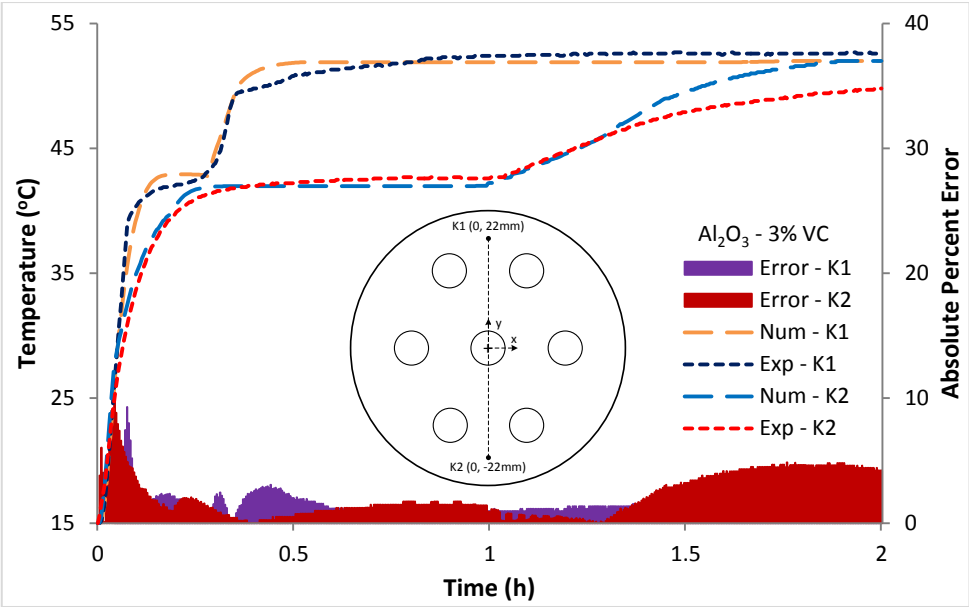

(A)

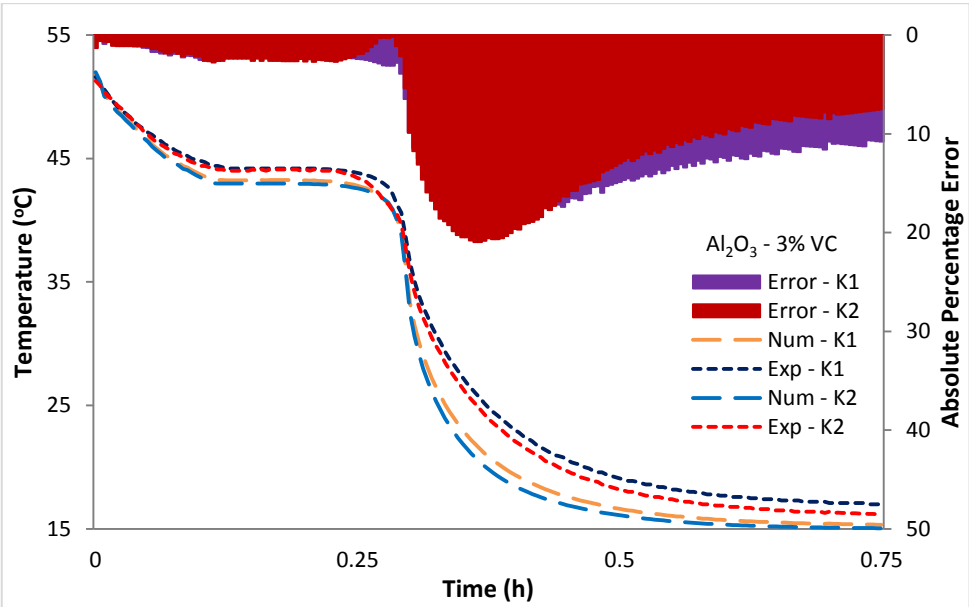

(B)

Fig. 5 Numerical results validation with experimental results by comparing temperature profiles at two positions in shell container (K1: Top and K2: Bottom): (A) charging cycles at 52 ^{o}C and (B) discharging cycles at 15 ^{o}C [28].

3. Results and Discussion

To provide a detailed insight into thermal performance of nano-PCM sample in heat exchanger and to reduce numerical simulation data, the thermal behaviour for MgO based nano-PCM samples are discussed. In later stages, the comparative thermal behaviour for all fourteen nano-particles materials are presented and discussed.

3.1. Charging/Melting Cycles

3.1.1. Thermal behaviour of MgO based nano-PCM

In case of charging cycles, the nano-PCM sample in heat exchanger is subjected to fixed inlet temperature of 52 ^{o}C. Liquid fraction of nano-PCM in shell container during the course of charging cycle is illustrated in **Fig. 6**. It is noticed that during the onset of charging cycle, thermal energy from inlet temperature boundaries are transferred to low temperature nano-PCM in shell container. Nano-PCM captures thermal energy and consequently increases the temperature. Melting process initiates as the latent portion of thermal energy is absorbed by nano-PCM. Liquefied nano-PCM surrounds the solid inlet temperature boundaries and takes their shape. During this stage, conduction is driving mode of heat transfer between inlet temperature boundaries and nano-PCM. In second stage, the quantity of liquefied nano-PCM increases and thus, the upward movement of high temperature and low density liquid molecules occurs due to buoyance induced natural convection. Increased upward movement of high temperature liquefied molecules promote higher charging rate in top portion of shell container as compared to lower portion, as shown in **Fig. 6 (A)** and **(B)**. During this stage, natural convection is the dominant mode of heat transfer. In final stage, the congestion of high temperature liquefied molecules at top portion of shell container results in re–circulation towards solid nano-PCM in lower portion. However, the high temperature liquefied molecule loses thermal energy to surrounding liquid molecules as it reaches the solid nano-PCM in lower portion. Hence, the phase transition rate is very slow in lower region of shell container, as shown in **Fig. 6 (C)** and **(D)**. During this stage, natural convection is controlling the heat transfer between liquefied and solid nano-PCM in lower portion of shell container. Moreover, the average liquid fraction of nano-PCM in shell container after charging for 10, 20, 30 and 40 min are 0.32, 0.66, 0.83 and 0.92, respectively. It confirms that the charging rate is higher at first and second stages, whereas it is relatively slower during final stage.

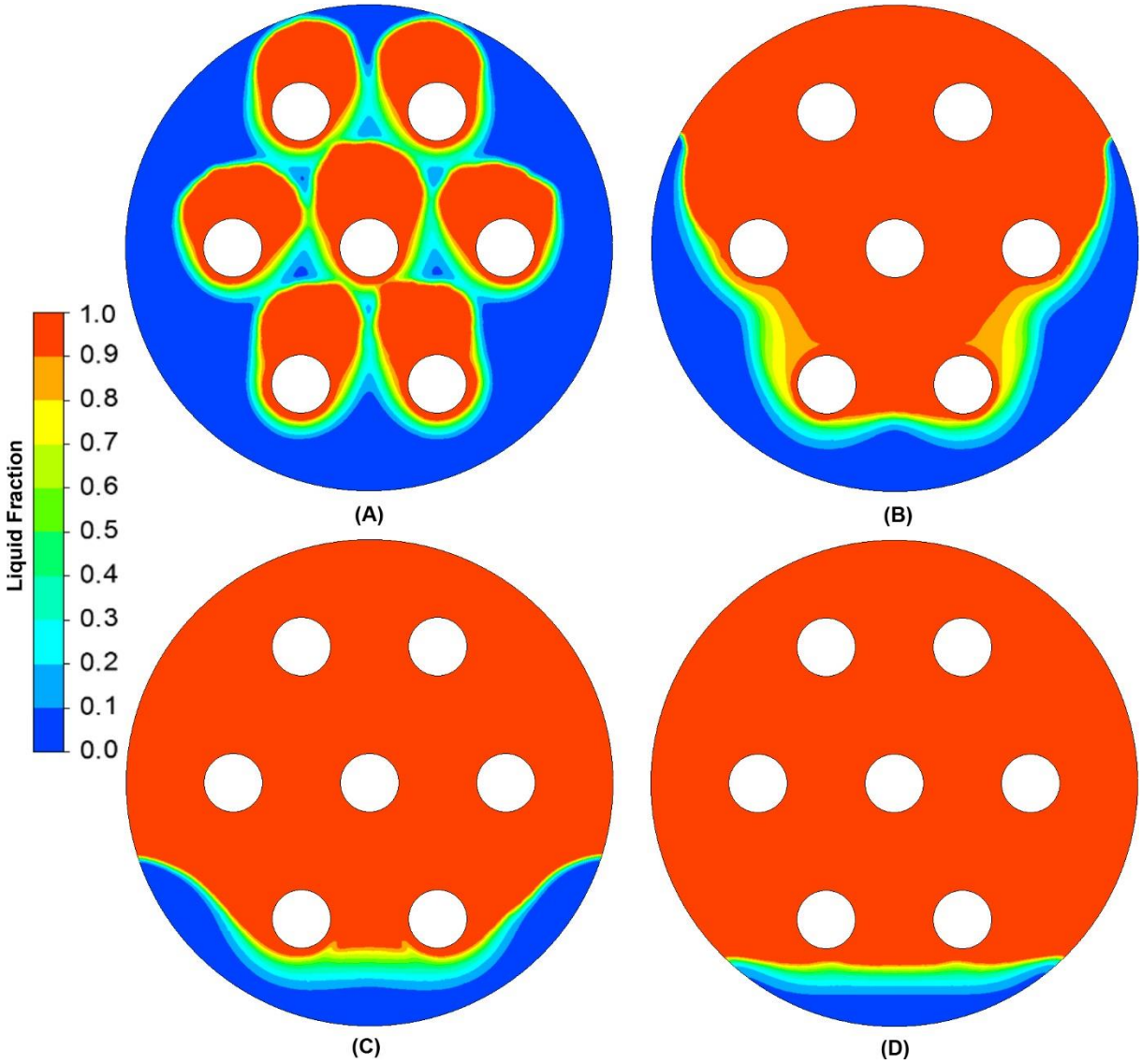

Fig. 6 Liquid fraction contours of nano-PCM sample with 1% volume concentration of MgO at different time intervals while charging at constant inlet temperature of 52 ^{o}C: (A) 10 min, (B) 20 min, (C) 30 min and (D) 40 min.

In similar manner, the velocity streamlines of nano-PCM in shell container during charging cycle are illustrated in **Fig. 7**. It can be noticed that after charging for 10 min, the liquefied nano-PCM forms high velocity vortex above the inlet temperature boundaries. As charging cycle progress, the melted quantity of nano-PCM increases and consequently the velocity streamlines develop and expand towards top portion of shell container, as shown in **Fig. 7 (B)**. The liquid fraction of nano-PCM increases which results in stratified liquid layers in top portion of shell container, as shown in **Fig. 7 (C)**. In final stages, the velocity streamlines are weak and almost identical, as shown in **Fig. 7 (D)**. The stratified liquid layers at top portion are reason for weaker heat transfer at lower portion of shell container. The average velocity of liquefied nano-PCM in shell container after charging for 10, 20, 30 and 40 min are 0.31, 0.67, 0.28 and 0.08 mm/s, respectively.

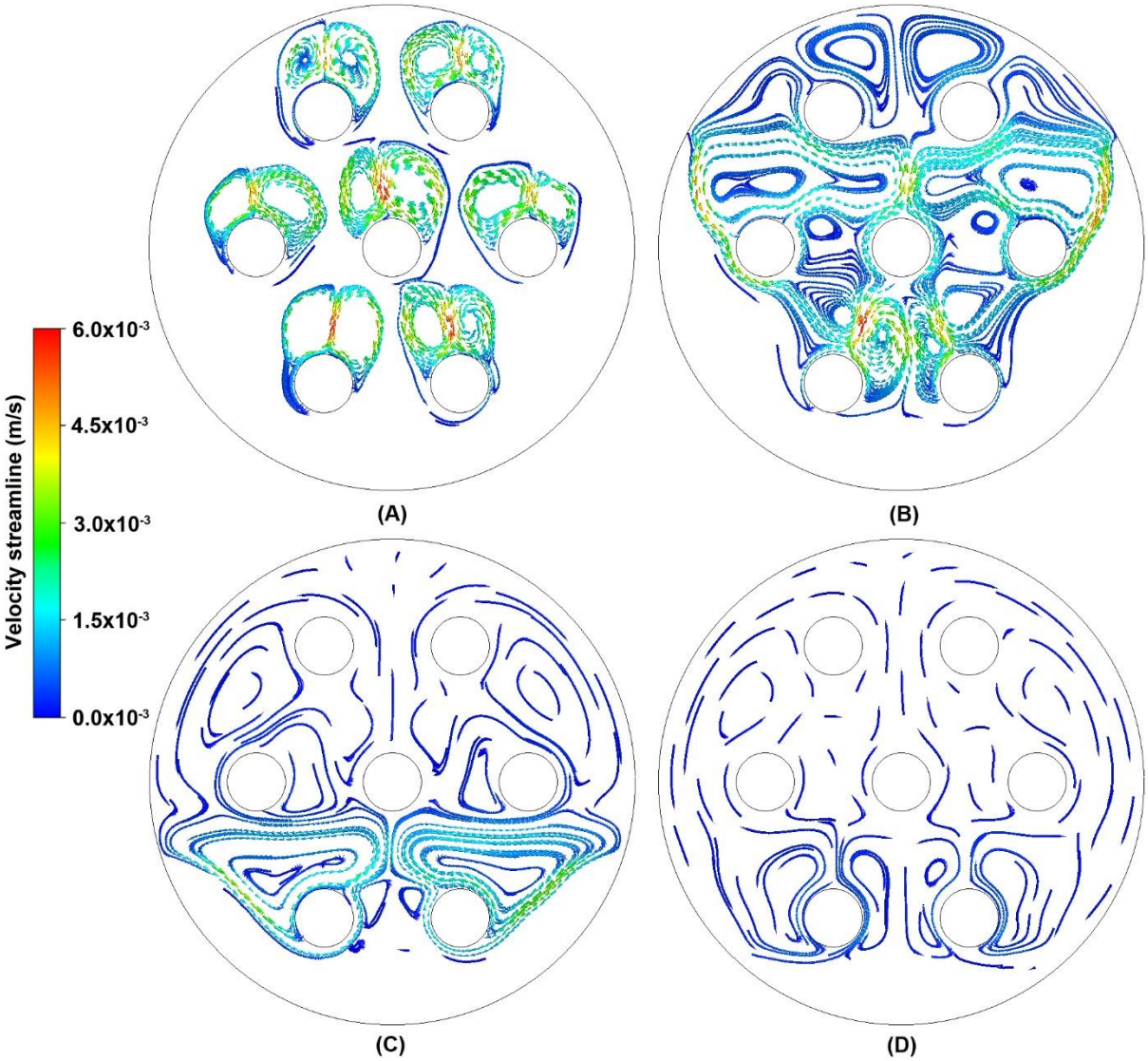

Fig. 7 Velocity streamlines of nano-PCM sample with 1% volume concentration of MgO at different time intervals while charging at 52 ^{o}C: (A) 10 min, (B) 20 min, (C) 30 min and (D) 40 min.

Natural convection has demonstrated significant impact on melting behaviour of nano-PCM in shell container. Non-dimensional numbers (i.e. Nu, Pr and Ra) are computed to quantify and help analyse natural convection effects on nano-PCM, as shown in **Fig. 8**. During charging process, the temperature of nano-PCM increases which causes reduction in dynamic viscosity and enhancement in effective thermal conductivity (see **Fig. 2**). The effect of viscous forces are quieten by improved thermal forces. In other words, Pr is reduced with the progression of charging cycle. Likewise, Ra is augmented with an increase in buoyancy driven natural convection. Also, Ra provides a criterion to evaluate the convectional instabilities during phase transition. Ra undergoes an irregular increase between $(0.1\,h \leq t \leq 0.25\,h)$ because natural convection controls the heat transfer between inlet temperature boundaries and solid nano-PCM. However, the upward rise of liquefied nano-PCM is still obstructed by solid nano-PCM. Therefore, the high velocity vortex above inlet temperature boundaries are generated (see **Fig. 7**) and consequently, Ra increases until entire mass of nano-PCM in top portion of shell container is melted, as shown in **Fig. 8 (A)**. As the liquefied nano-PCM layers stratify in top portion of shell container, a relatively stable reduction in natural convection is noticed. Furthermore, Nu increases with augmented Ra, due to

improved natural convection as compared to conduction heat transfer. Non-linear regression technique is adopted to generate correlation between Nu–Ra, as given in **Fig. 8 (B)**. The constant $(C = 0.217)$ and exponent $(n = 0.318)$ of generated correlation are in close congruence with the results produced by Morgan [66] for horizontal cylinder.

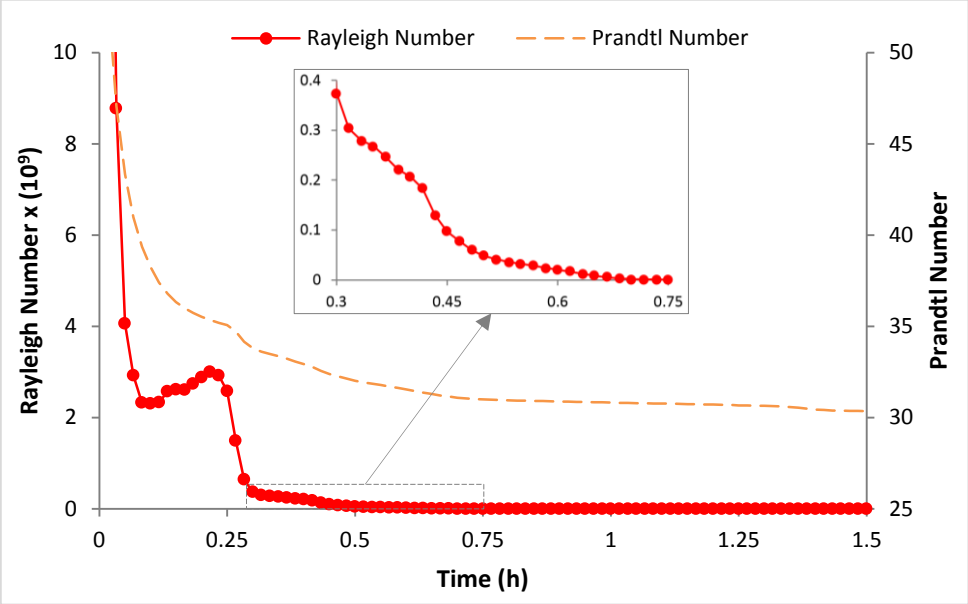

(A)

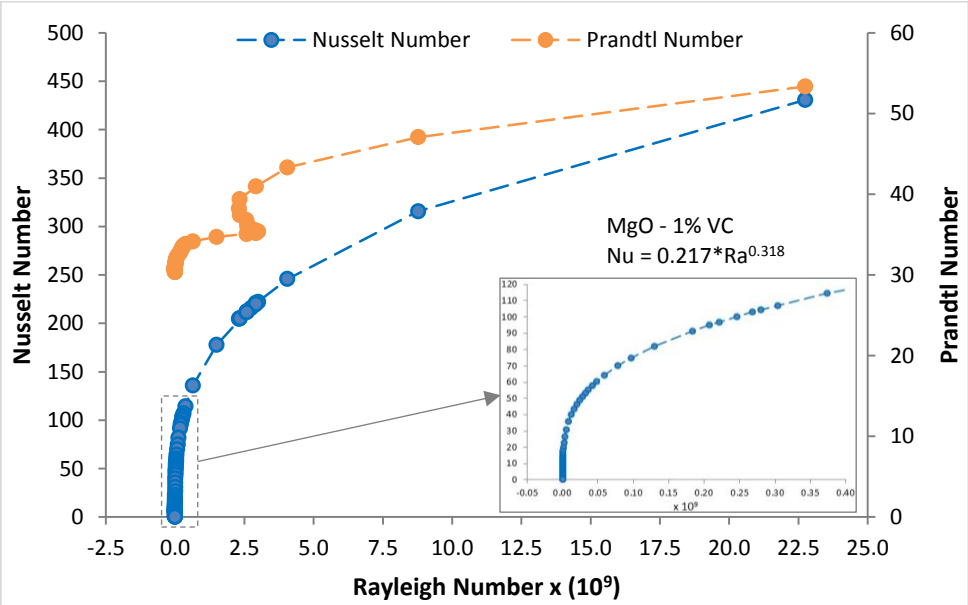

(B)

Fig. 8 Non-dimensional Ra, Nu and Pr numbers for MgO – 1% VC based nano-PCM sample in shell container during charging cycle: (A) Ra and Pr versus time and (B) Nu and Pr versus Ra.

Heat flux and liquid fraction response to melting process of nano-PCM samples with different volume concentration are plotted in **Fig. 9**. As discussed earlier, the melting process is divided into three different stages. In earlier stages, the heat flux ascends until it reaches the peak value and then follows by a rapid decline. The peak heat flux is slightly increased with an increase in volume concentration. Inclusion of higher concentration of nano-particles increases the effective thermal conductivity, which results in higher peak heat flux. This stage is mainly dominated by conduction heat transfer. In second stage, the earlier decline in

heat flux from previous stage is followed by a moderate increase until it reaches the second peak value. The earlier decline in heat flux is due to thermal resistance offered by liquefied nano-PCM around inlet temperature boundaries. Heat flux reaches to second peak due to perpetual escalation of natural convection in liquefied nano-PCM. In this stage, the liquid fraction curves illustrate a relatively moderate enhancement with increasing concentration of nano-particles. Also, until the end of second stage, the liquid fraction curves for all samples have presented a rapid and almost linear increase. In third stage, the heat flux sustains a gradual decline due to reduction of temperature gradient, stratification of liquefied layers in top portion and weaker thermal and momentum diffusion. As a result, the liquid fraction undergoes a relatively slower increase, which is depicted by logarithmic nature of liquid fraction curve. Heat flux value approaches zero after achieving thermal equilibrium between inlet temperature boundaries and nano-PCM. Inclusion of higher volume concentration of nano-particles has demonstrated improved melting rate. For instance, the total melting time is reduced from 1.36 h to 1.21 h with an increase in volume concentration from 1% – 5%, respectively. Furthermore, the impact of increasing volume concentration of nano-particles on non-dimensional Nu and heat transfer coefficient is evident from **Fig. 10**. It can be noticed that with inclusion of higher concentration, both Nu and heat transfer coefficient decrease which represents that conductive heat transfer relatively strengthens with higher concentration.

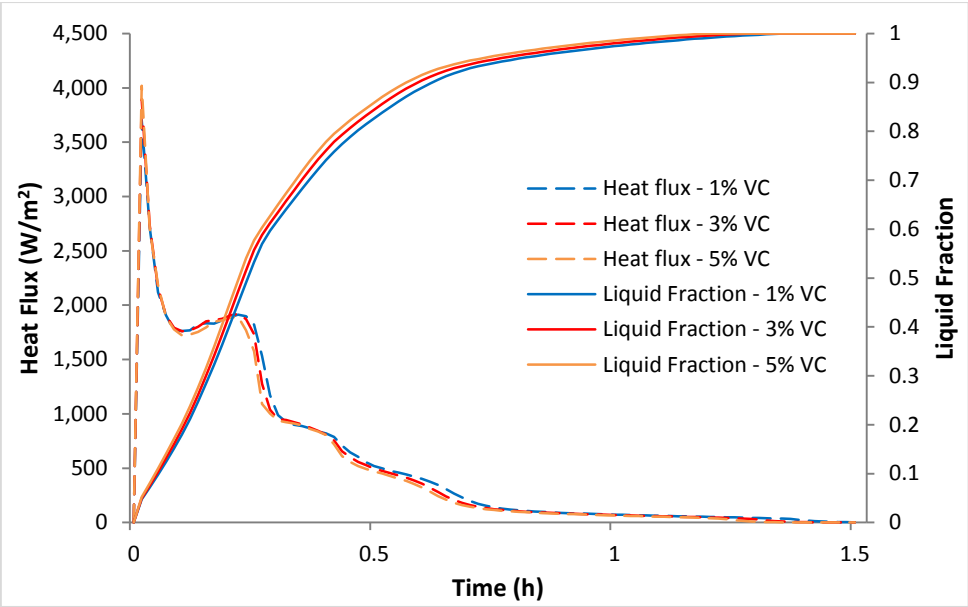

Fig. 9 Heat flux and liquid fraction of MgO based nano-PCM samples during charging process.

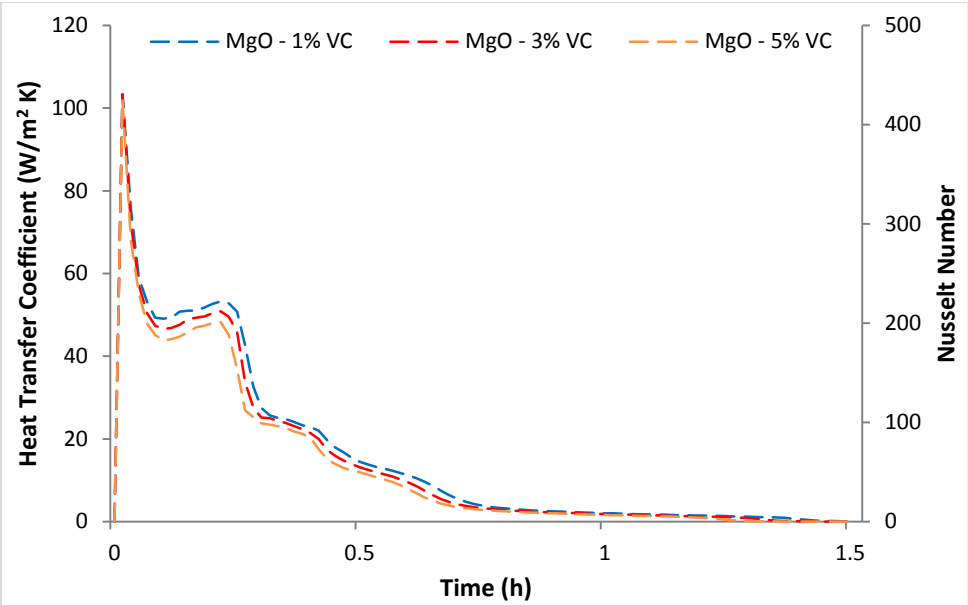

Fig. 10 Heat transfer coefficient and Nusselt number of MgO based nano-PCM samples during charging process.

3.1.2. Thermal behaviour of all nano-PCM samples

In this section, the impact of all nano-particles materials with three different volume concentrations on charging rate, total enthalpy and heat transfer performance of nano-PCM are discussed. Inlet temperature for all charging cycles are kept constant at 52 ^{o}C. Inclusion of metal-oxides nano–particles increase the effective thermal conductivity and surface area for heat transfer. Hence, the charging rate of nano-PCM in shell container can be enhanced.

The average melting time for all nano-PCM samples and their respective percentage enhancement in charging rate as compared to base paraffin are illustrated in **Fig. 11**. In case of 1% volume concentration, the average melting time is significantly reduced from 1.58 h to 1.22 h for SiO_2 based nano-PCM as compared to base paraffin. Thus, the charging rate is significantly augmented by 29.45% for SiO_2 based nano-PCM as compared to base paraffin, as shown in **Fig. 11 (A)**. Similarly, Al_2O_3, MgO and NiO based nano-PCM samples have exhibited consecutively higher charging rate as compared to other metal-oxides. In case of 3% volume concentration, the respective enhancement in charging rates for SiO_2 and Al_2O_3 based nano-PCM samples are standout with 35% and 26%, as shown in **Fig. 11 (B)**. In case of 5% volume concentration, the average melting time for SiO_2, Al_2O_3 and MgO based nano-PCM samples are significantly reduced to 1.12 h, 1.18 h and 1.20 h, respectively. Similarly, the respective charging rates are enhanced by 41.04%, 33.10% and 31.25% as compared to base paraffin, as shown in **Fig. 11 (C)**. Irrespective of higher thermal conductivity of Al_2O_3, MgO and ZnO nano-particles as compared to SiO_2 (refer to **Table 2**), the effective thermal conductivity and charging rates of SiO_2 based nano-PCM are higher. The reason behind is the lower density of SiO_2 nano-particles, which allows to accommodate more nano-particles in base paraffin for a given volume concentration. As a result, the effective surface area and Brownian motion for heat transfer are significantly improved, which can generate higher charging rates [65].

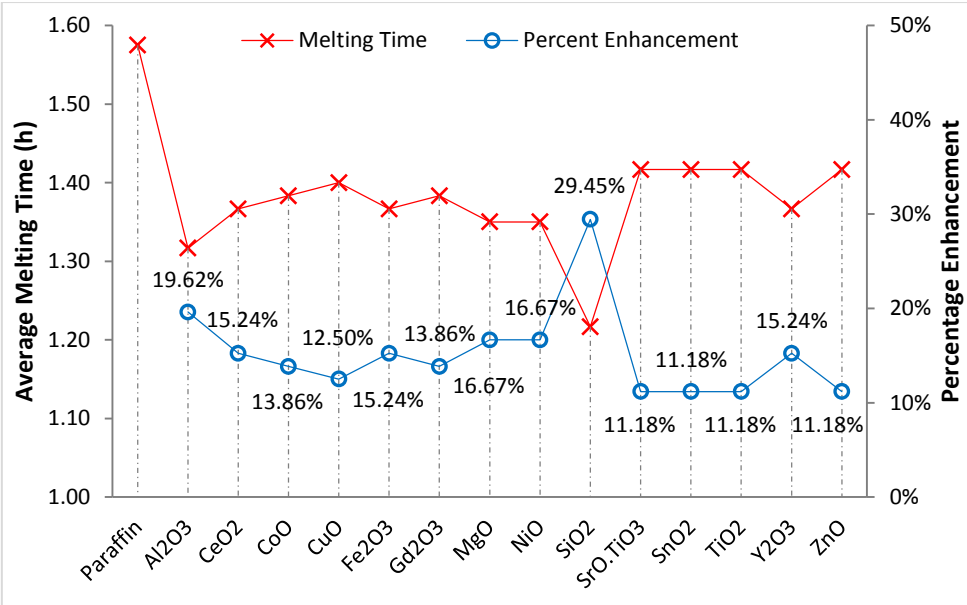
Melting Time
Percent Enhancement
Average Melting Time (h)
Percentage Enhancement
1.60
1.50
1.40
1.30
1.20
1.10
1.00
50%
40%
30%
20%
10%
0%
19.62%
15.24%
13.86%
12.50%
15.24%
13.86%
16.67%
16.67%
29.45%
11.18%
11.18%
11.18%
15.24%
11.18%
Paraffin
Al2O3
CeO2
CoO
CuO
Fe2O3
Gd2O3
MgO
NiO
SiO2
SrO.TiO3
SnO2
TiO2
Y2O3
ZnO

(A)

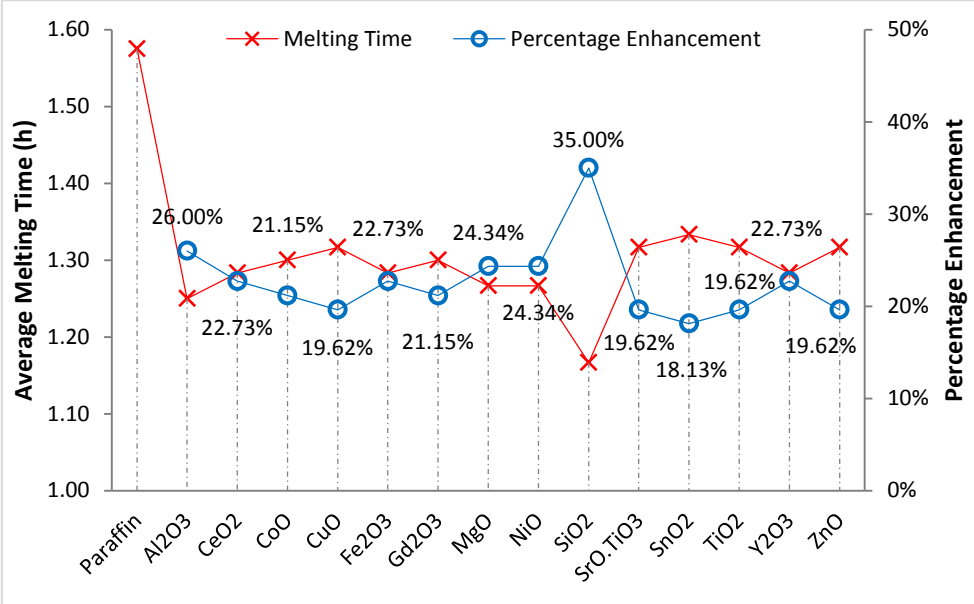
Melting Time
Percentage Enhancement
Average Melting Time (h)
Percentage Enhancement
1.60
1.50
1.40
1.30
1.20
1.10
1.00
50%
40%
30%
20%
10%
0%
26.00%
22.73%
21.15%
19.62%
22.73%
21.15%
24.34%
24.34%
35.00%
19.62%
18.13%
19.62%
22.73%
19.62%
19.62%
Paraffin
Al2O3
CeO2
CoO
CuO
Fe2O3
Gd2O3
MgO
NiO
SiO2
SrO.TiO3
SnO2
TiO2
Y2O3
ZnO

(B)

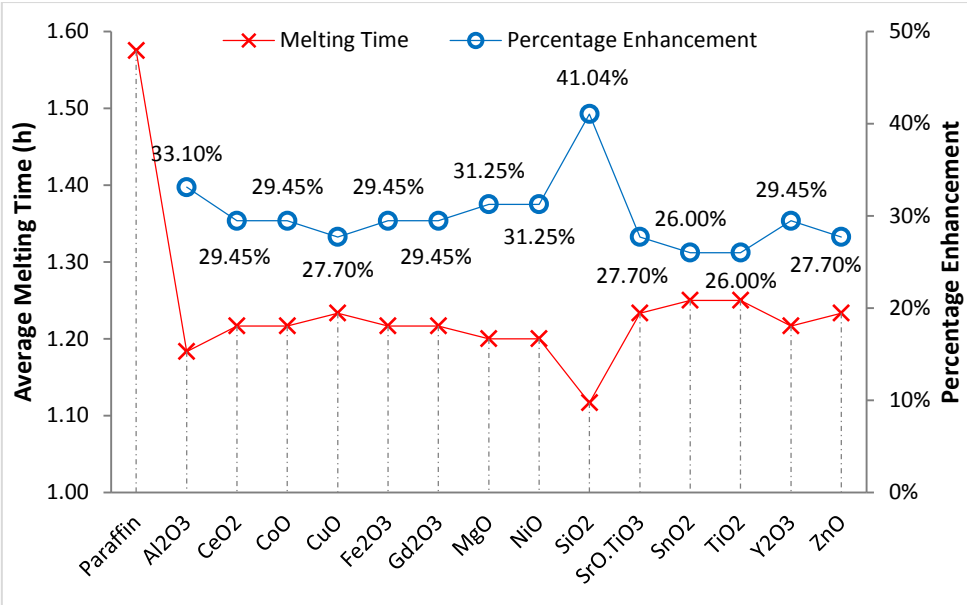

(C)

Fig. 11 Average melting time of nano-PCM samples with three volume concentrations and respective percentage enhancement in charging rate as compared to base paraffin: (A) 1%, (B) 3% and (C) 5%.

Heat transfer between inlet temperature boundaries and nano-PCM increases the overall thermal enthalpy of nano-PCM. Transient behaviour of total enthalpy for all nano-PCM samples are illustrated in **Fig. 12**. Due to higher heat flux at earlier stages of charging cycles, the nano-PCM samples capture thermal energy at higher rate as illustrated by linear increment in overall enthalpy. However, as the heat flux weakens due to accumulation of liquefied layers in top portion of shell container, the thermal diffusion also reduces which effects the rate of thermal energy storage. Therefore, the overall enthalpy curve illustrates a logarithmic increase until a thermal equilibrium is achieved between inlet temperature and nano-PCM. Moreover, the volume for base paraffin in heat exchanger with control volume is compromised with the inclusion of nano-particles, which results in reduced thermal enthalpy as compared to pure paraffin. Hence, there is trade-off between optimum charging rate enhancement and overall enthalpy reduction. In case of 1% volume concentration, SiO_2, Al_2O_3, MgO and TiO_2 based nano-PCM samples have presented consecutively higher overall thermal enthalpy as compared to other metal-oxides, ranging from 297.8 – 291.2 kJ/kg. Percentage reduction in overall enthalpy, as compared to base paraffin, range from 3.12% – 5.27%. In contrast, the inclusion of Gd_2O_3 nano-particles have illustrated the lowest overall enthalpy, with percent reduction of 9.34%, as shown in **Fig. 12 (A)**. Likewise, in case of 3% and 5% volume concentration, SiO_2, Al_2O_3 and MgO based nano-PCM samples have remained the suitable candidates, with overall enthalpy ranging from 277.1 – 267.4 kJ/kg and 258.3 – 244.3 kJ/kg, respectively. However, the total enthalpy for Gd_2O_3 based nano-PCM samples with 3% and 5% volume concentrations have significantly reduced by 24.53% and 35.78%, respectively (see **Fig. 12 (B)** and **(C)**). Furthermore, the enthalpy distributions in shell container for nano-PCM samples with 5% volume concentrations after charging at constant 52 ^{o}C for 25 min are illustrated in **Fig. 13**. It is construed that the thermo-physical characteristics of nano-particles such as density, heat capacity and thermal conductivity have shown significant influence on overall thermal enthalpy of nano-PCM. Hence, the metal-oxides with smaller density and higher thermal conductivity and heat capacity are preferable due to their tendency of generating significant enhancement in charging rate with

acceptable reduction in overall enthalpy. **Table 3** lists the time average of enthalpy, heat flux, velocity and non-dimensional Pr and Nu for all three volume concentrations based nano-PCM samples.

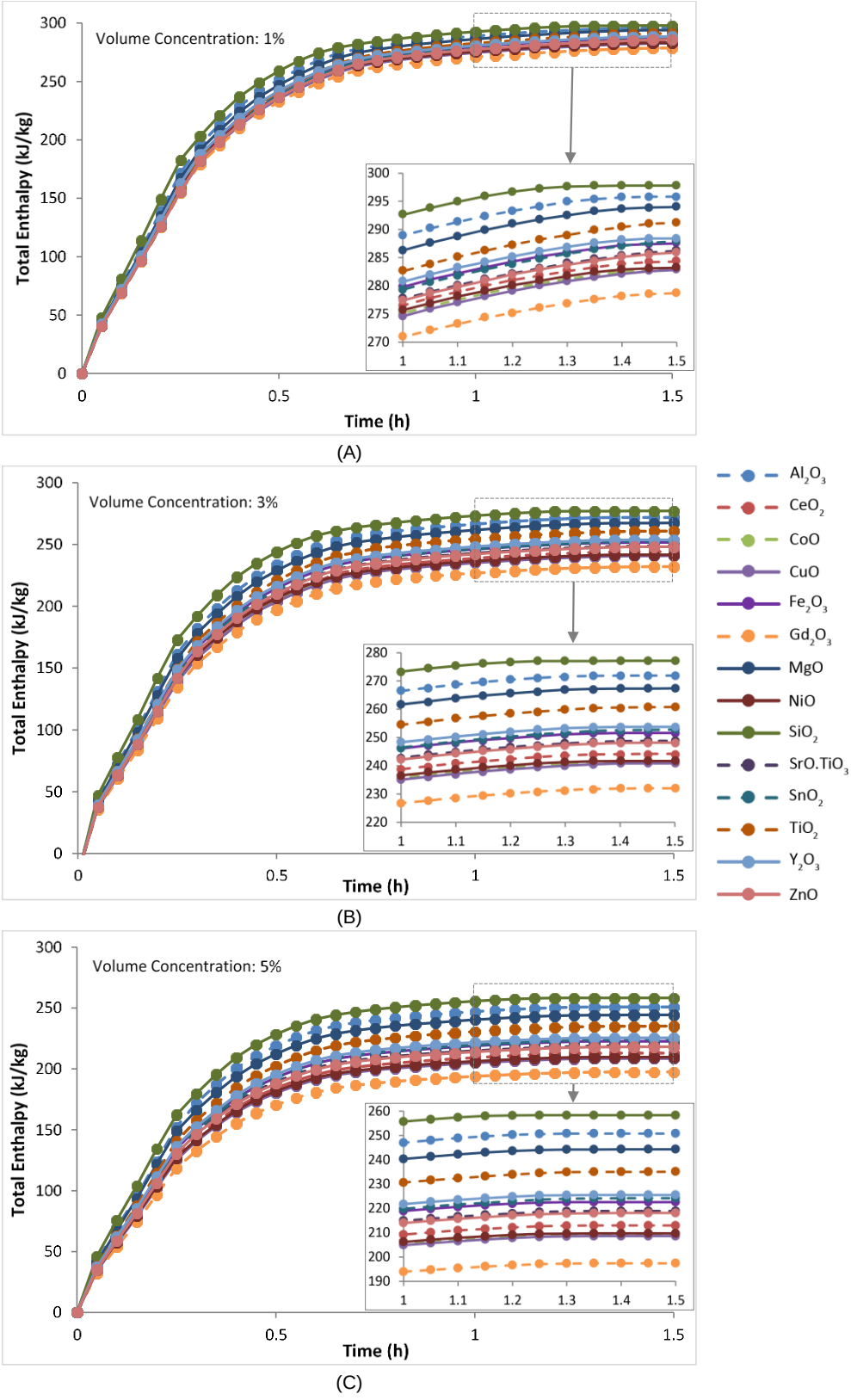

Fig. 12 Total enthalpy of nano-PCM samples during charging cycles with different volume concentrations: (A) 1%, (B) 3% and (C) 5%.

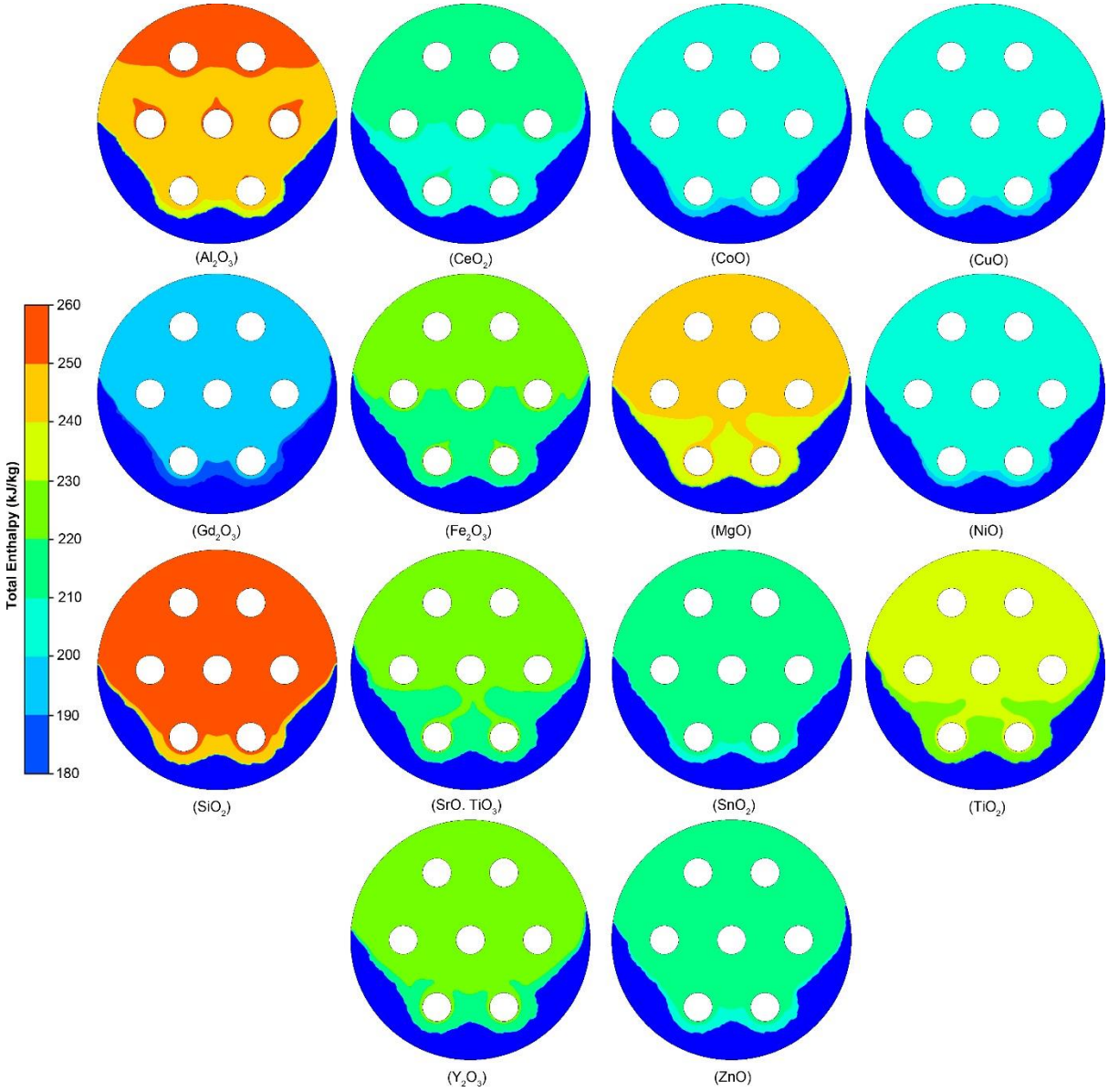

Fig. 13 Enthalpy contours of nano-PCM samples with 5% volume concentration after charging for 25 min.

Table 3
Average values derived from charging cycles of nano-PCM samples with three volume concentrations.

Nano-PCM	Enthalpy (kJ/kg)			Heat flux (W/m^2)			Heat Transfer Coefficient ($W/m^2 K$)			Velocity (mm/s)			Prandtl Number			Nusselt Number		
	1%	3%	5%	1%	3%	5%	1%	3%	5%	1%	3%	5%	1%	3%	5%	1%	3%	5%
Al_2O_3	295.8	271.9	250.8	561.92	551.53	539.54	15.19	14.91	14.59	0.179	0.171	0.160	32.16	32.60	34.09	62.74	58.68	54.43
CeO_2	284.3	244.2	212.9	559.40	543.39	526.20	15.12	14.69	14.23	0.184	0.169	0.160	32.74	30.67	29.75	66.30	61.27	56.28
CoO	282.9	241.2	209.0	559.07	542.48	525.86	15.11	14.67	14.22	0.181	0.170	0.160	32.69	30.41	29.34	66.46	61.36	56.45
CuO	282.8	240.9	208.6	558.01	543.04	524.90	15.09	14.68	14.19	0.179	0.170	0.161	33.08	30.02	28.09	67.76	62.58	57.30
Gd_2O_3	278.7	232.0	197.4	557.95	541.77	523.97	15.08	14.65	14.17	0.179	0.170	0.159	32.46	29.54	27.95	66.84	61.74	56.64
Fe_2O_3	287.5	251.6	222.6	559.23	543.61	527.43	15.12	14.70	14.26	0.178	0.171	0.162	32.84	31.33	30.84	65.76	60.83	55.99
MgO	294.0	267.4	244.3	559.52	545.02	527.43	15.13	14.73	14.32	0.181	0.172	0.162	33.01	32.41	32.55	64.92	60.10	55.31
NiO	283.2	241.7	209.7	556.07	541.66	525.99	15.09	14.64	14.22	0.180	0.167	0.158	32.26	30.67	30.46	64.90	59.97	55.24
SiO_2	297.8	277.1	258.3	559.64	542.48	527.08	15.13	14.67	14.25	0.175	0.165	0.151	30.27	32.86	37.46	57.19	53.15	49.12
$SrO.TiO_3$	286.2	248.8	218.9	558.65	543.08	527.35	15.10	14.68	14.26	0.179	0.172	0.166	33.72	30.43	28.04	69.03	63.58	58.42
SnO_2	287.9	252.8	224.2	558.48	543.06	527.99	15.10	14.68	14.27	0.181	0.173	0.167	33.91	31.04	28.95	68.99	63.84	58.97
TiO_2	291.2	260.8	235.1	558.46	545.40	528.99	15.10	14.74	14.30	0.182	0.171	0.165	34.05	31.71	30.00	68.52	63.59	58.51
Y_2O_3	288.4	253.8	225.5	558.71	543.47	527.47	15.10	14.69	14.26	0.179	0.170	0.161	32.85	31.50	31.13	65.52	60.65	55.82
ZnO	285.9	248.2	218.1	558.37	543.16	527.57	15.10	14.68	14.26	0.181	0.170	0.166	33.71	30.37	27.97	69.03	63.63	58.48

3.2. Discharging/Solidification Cycles

3.2.1. Thermal behaviour of MgO based nano-PCM

Thermal performance enhancement of discharging cycles are equally essential for promising large-scale practical utilisation. During discharging cycles, the high temperature liquid nano-PCM in shell container release thermal energy to low temperature water in tubes, which are set to constant 15 ^{o}C. As a result, the phase transition of nano-PCM from liquid to solid begins. Liquid fraction of nano-PCM in shell container reduces with the formation of solidified layers, as illustrated in **Fig. 14**. At earlier stages, the liquid nano-PCM in close proximity to inlet boundaries release latent portion of thermal energy and forms a symmetrical thin solid layer around the tubes boundaries. Thickness of solidified layers increase with the course of discharging cycle, which yields an improved thermal resistance to discharging process. Moreover, as the discharging cycle progress, the temperature gradient between inlet boundaries and nano-PCM decreases which is another reason for slower discharging rate at later stages. The reduction in average liquid fraction of nano-PCM after discharging for 5, 10, 15 and 20 min are noticed to be 0.30, 0.15, 0.07 and 0.02, respectively. It confirms that the discharging rate is higher at earlier stages and weaker at later stages due to formation of low thermal conductive solidified layers around the inlet boundaries. Furthermore, the liquid fraction contours indicate an insignificant impact of natural convection, whereas conduction remained the dominant mode of heat transfer at both earlier and later stages of discharging cycle.

Likewise, the temperature contours of nano-PCM in shell container for discharging cycle are illustrated in **Fig. 15**. It can be noticed that due to cluster of inlet temperature boundaries, the liquid nano-PCM in centre of shell container experience rapid thermal energy discharge as compared to nano-PCM closer to exterior boundary of shell container. The symmetrical temperature contours in both lower and top portion of shell container confirms the insignificant natural convection and dominant conduction heat transfer throughout the discharging cycle. Although, the velocity contours illustrated a slight upward movement of relatively higher temperature liquid nano-PCM, however the impact on solidification rate is insignificant due to geometrical distribution of tubes in shell container. The earlier formation of solidified layers around the tubes in centre of shell container confines the upward propagation of higher temperature liquid nano-PCM. Hence, the liquid nano-PCM is trapped in areas adjacent to exterior boundary of shell container and it requires more time to release thermal energy and undergo phase transition. As illustrated in **Fig. 15 (D)**, the nano-PCM in centre of shell container is completely solidified and records temperature at 15 ^{o}C, whereas the nano-PCM areas adjacent to exterior boundary are in mushy zone and records temperature ranging from 42 – 45 ^{o}C.

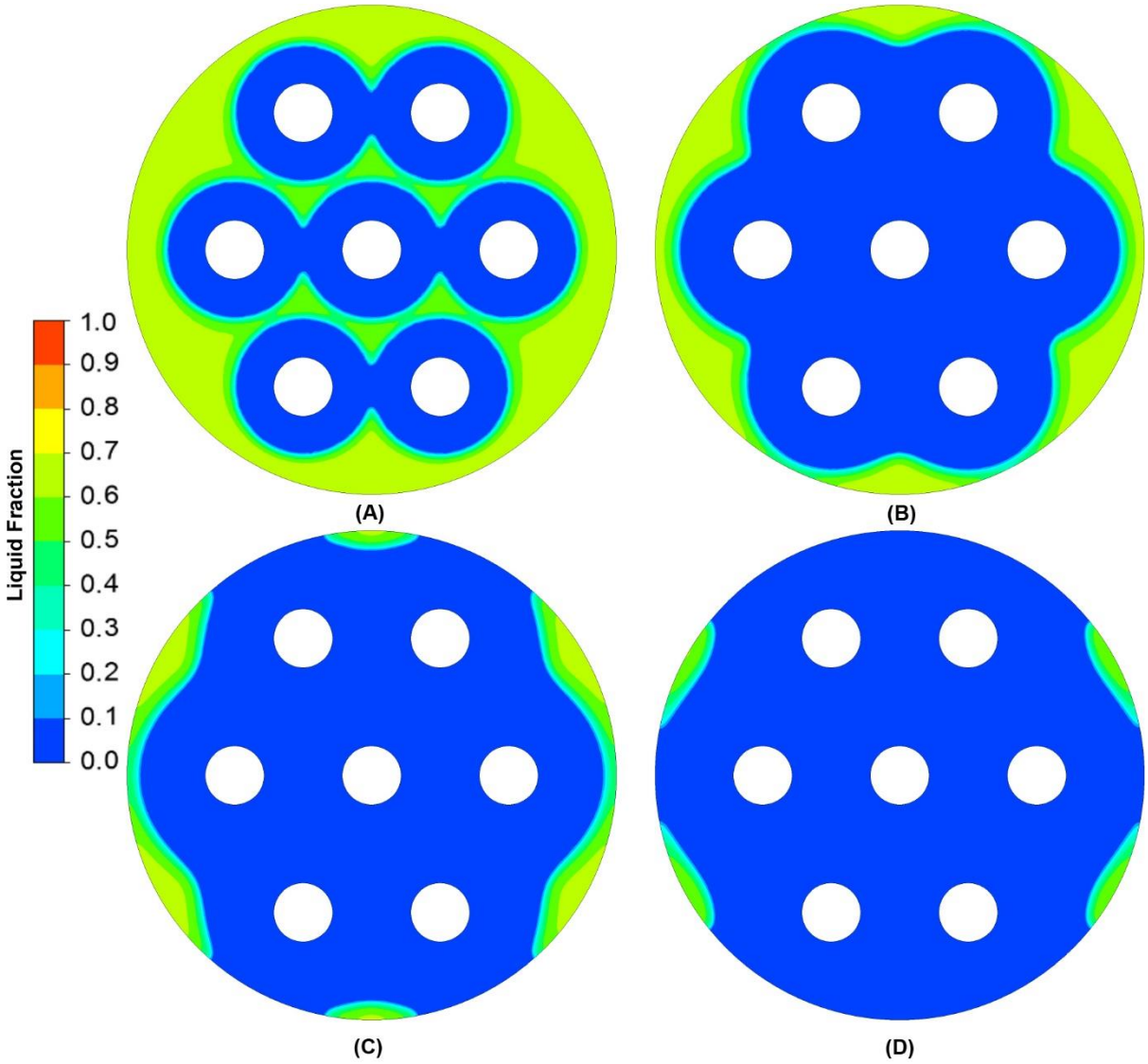

Fig. 14 Liquid fraction contours of nano-PCM sample with 1% volume concentration of MgO at different time intervals while discharging at constant inlet temperature of 15 ^{o}C: (A) 5 min, (B) 10 min, (C) 15 min and (D) 20 min.

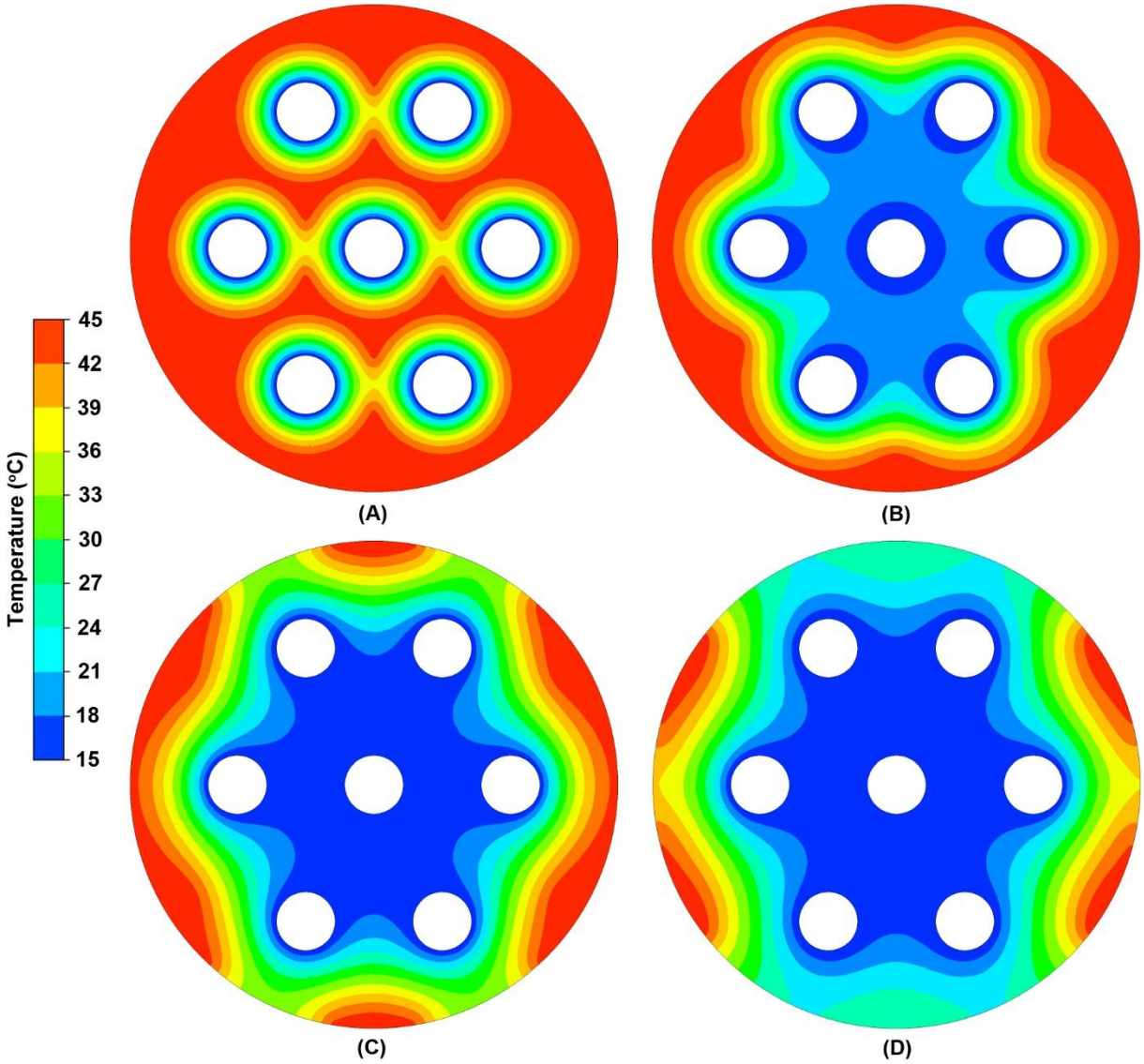

Fig. 15 Temperature contours of nano-PCM sample with 1% volume concentration of MgO at different time intervals while discharging at 15 ^{o}C: (A) 5 min, (B) 10 min, (C) 15 min and (D) 20 min.

Heat flux and liquid fraction response to discharging cycles of nano-PCM samples with different volume concentration are illustrated in **Fig. 16**. To indicate discharging process, the heat flux is plotted in negative. As previously described, the discharging cycle is divided into three main stages. In earlier stages, the discharging heat flux increases until a peak value is reached and then a rapid declination in follow-up. It can be noticed that the peak discharging heat flux is significantly increased with an increase in volume concentration. The reasons behind are the relatively higher effective thermal conductivity with an increase in volume concentration and conduction dominant heat transfer. Increase in effective thermal conductivity improves the conduction heat transfer rate and as a result, a significant enhancement in peak discharging heat flux is achieved. Likewise, the liquid fraction plots have shown an abrupt linear declination from 1 to almost 0.5, which indicates that almost half mass of nano-PCM has undergone phase transition from liquid to solid. In second stage, the discharging heat flux appears to follow a moderate declination ranging from 4500 – 2000 W/m^2. During this stage, the temperature gradient between nano-PCM and inlet temperature decreases and the formation of solidified nano-PCM around inlet boundaries weakens the

heat flux. Liquid fraction also illustrate a similar moderate reduction due to weakened heat flux. In third stage, the discharging heat flux endure a gradual reduction due to smaller temperature gradient and continuous growth in thickness of solidified nano-PCM around inlet temperature boundaries. Due to which, the liquid fraction indicates a slower logarithmic reduction until solidification is completed.

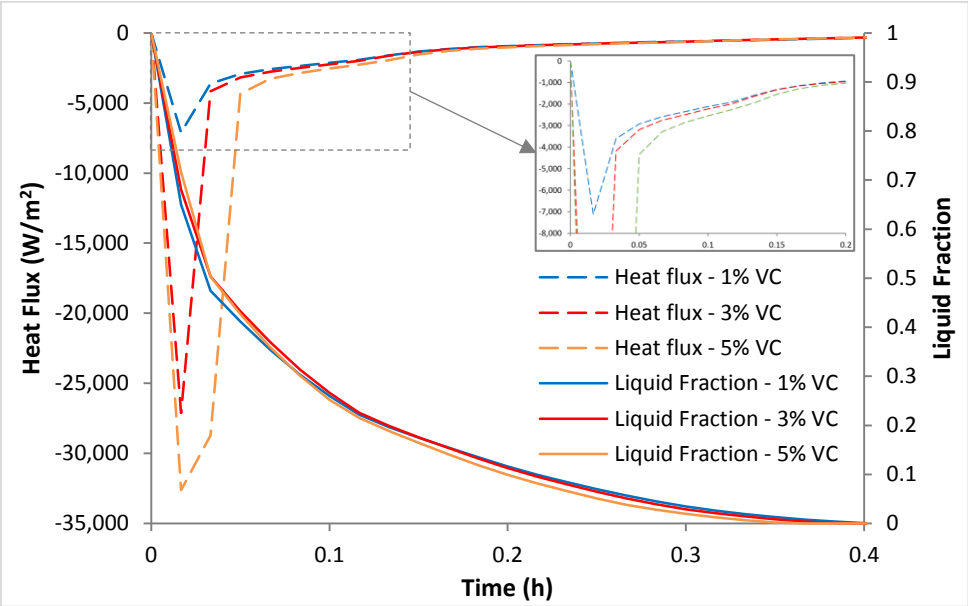

Fig. 16 Heat flux and liquid fraction of MgO based nano-PCM samples during discharging cycles.

3.2.2. Thermal behaviour of all nano-PCM samples:

In this section, the comparative enhancement in discharging rates of metal-oxides based nano-PCM with three volume concentrations are examined. The adiabatic exterior boundary of shell container ensures no thermal losses to surrounding and therefore, the total enthalpy charged by nano-PCM is available for discharge to low temperature water. Total enthalpy of all nano-PCM samples with varied volume concentrations are listed in **Table 3**. As previously discussed, the inclusion of nano-particles to base paraffin in a control volume is a trade-off between an enhancement in discharging rate and reduction in total enthalpy.

Average solidification time and percentage enhancement in discharging rate of nano-PCMs with three volume concentrations are compared to base paraffin, as shown in **Fig. 17**. For 1% volume concentration, the average solidification time is reduced from 27.75 min for base paraffin to 22.92, 24.0 and 24.5 min for SiO_2, Al_2O_3 and MgO based nano-PCM samples, respectively. Hence, the discharging rate is significantly enhanced by 21.09%, 15.63% and 13.27%, respectively. Likewise, for 3% and 5% volume concentrations, SiO_2 based nano-PCM samples have illustrated exceptional discharging performance, with enhancement in discharging rate of 26.62% and 30.08%, respectively. Whereas, the percentage enhancement for Al_2O_3 and MgO based nano-PCM samples seem inferior to Gd_2O_3 based nano-PCM. The reason behind is that due to inclusion of higher density nano-particles, the total enthalpy of nano-PCM reduces (see **Fig. 12**). Therefore, it requires relatively lesser solidification time to discharge the comparatively smaller total enthalpy. For instance, in case of 5% volume concentration, the Gd_2O_3 based nano-PCM requires 21.67 min to discharge 197.4 kJ/kg of thermal enthalpy, whereas, Al_2O_3 based nano-PCM requires 22.67 min to

discharge 250.8 kJ/kg of thermal enthalpy. In other words, to discharge equal amount of thermal energy (195 kJ/kg), the discharge time required for SiO_2, Al_2O_3, MgO, TiO_2 and Gd_2O_3 based nano-PCM samples with 5% volume concentrations are 7.34, 8.5, 9.42, 10.08 and 18.58 min, respectively. Therefore, the significance of discharging higher capacity of thermal enthalpy at higher discharging rate identifies SiO_2, Al_2O_3, MgO and TiO_2 as preferable candidates.

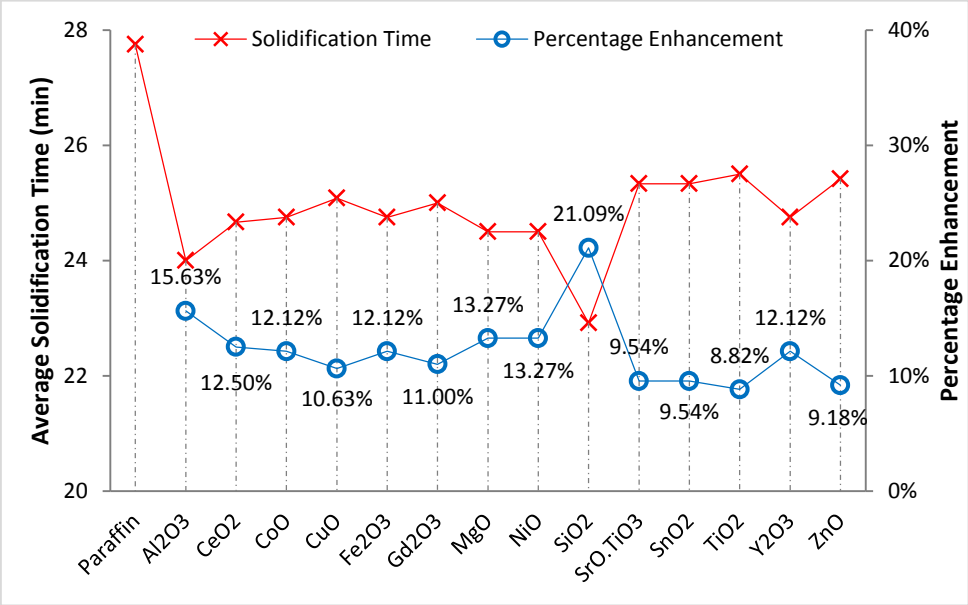

(A)

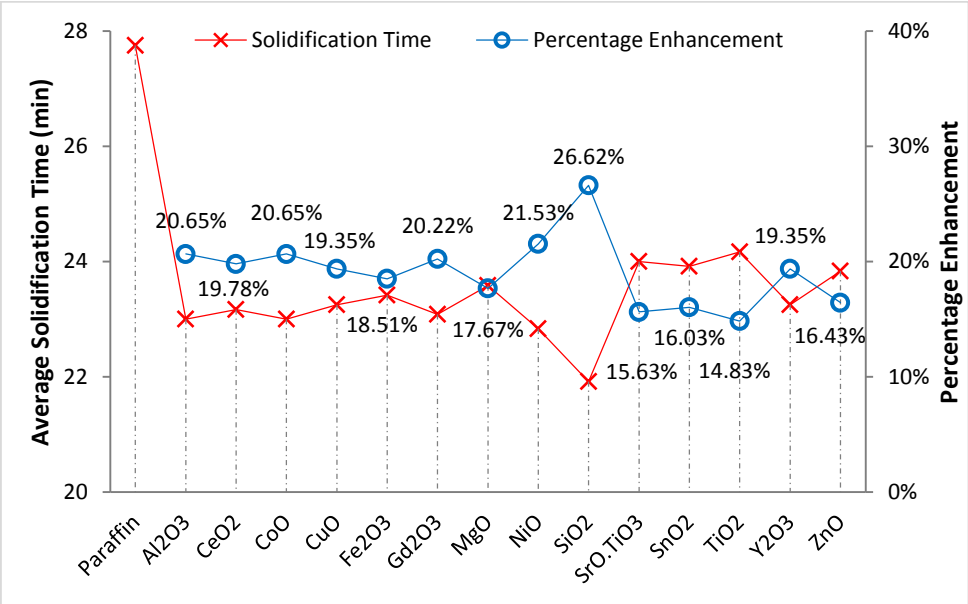

(B)

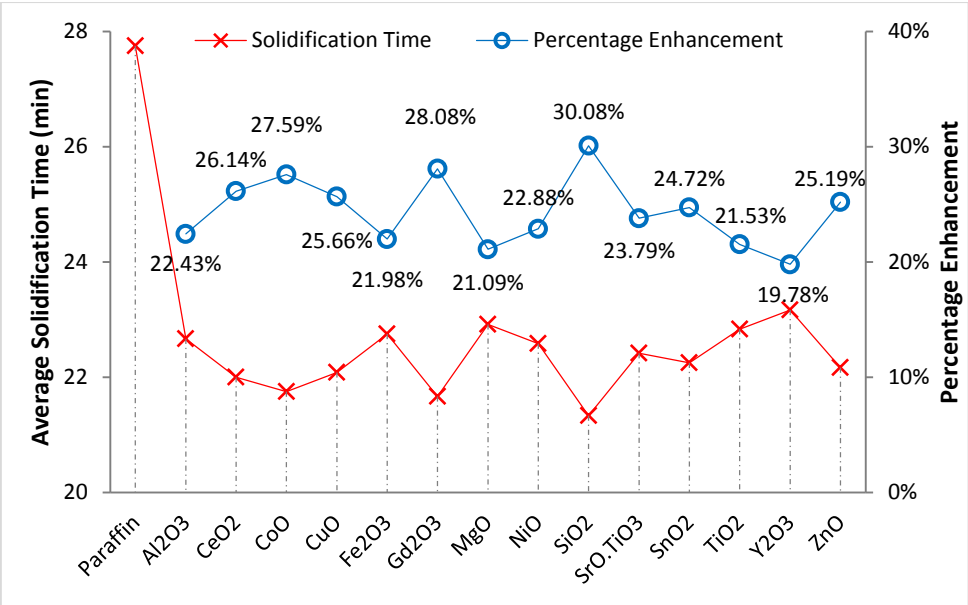

(C)

Fig. 17 Average solidification time of nano-PCM samples and percentage enhancement in discharging rate as compared to base paraffin: (A) 1% VC, (B) 3% VC and (C) 5% VC.

3.3. Economic evaluation of nano-PCM

It is construed from numerical simulations that the charging and discharging rates of base paraffin can be significantly enhanced with inclusion of nano-particles at the cost of reduction in total enthalpy. Likewise, the inclusion of expensive metal-oxides nano-particles will increase the total cost of nano-PCM. **Table 4** provides a comparison between all fourteen metal-oxides based nano-PCM in terms of required weight of nano-particles and respective elevation in price of nano-PCM with three volume concentrations. The required weight of nano-particles for respective metal-oxides and volume concentration is evaluated as:

$$w_{np} = \left(\frac{\Phi_{VC}}{100 - \Phi_{VC}}\right)\left(\rho_{np} V_{npcm}\right) \times 100 \tag{15}$$

Base paraffin (RT44HC) and metal-oxides prices are taken from Rubitherm [48] and IoLiTec nanomaterials [50], as listed in **Table 2**. In cost calculations, the price of nano-particles per gram is multiplied with the required weight of nano-particles for respective volume fraction. The calculated cost of nano-particles is then added to cost of base paraffin to evaluate total price of nano-PCMs (per kg).

It can be noticed that the total cost of nano-PCM elevates significantly with inclusion of nano-particles. For instance, the percent increase in total cost of nano-PCM ranges from 115% – 14085% for 1% volume concentration, 350% – 43125% for 3% volume concentration and 599% – 73386% for 5% volume concentration, respectively. In addition to significant enhancement in charging/discharging rates and minimal reduction in total enthalpy by SiO_2, Al_2O_3, MgO and TiO_2 based nano-PCMs, the price-performance ratios for all three volume concentrations are lower as compared to other listed metal-oxides. Therefore, these four metal-oxides can be recommended for utilisation as nano-additives in LHS systems.

Table 4
Price valuation of nano-PCMs with three volume concentrations and price-performance ratio for 5% - nano-PCMs.

Nano-PCM	Price of nano-particles (€/g)	1% Volume Concentration		3% Volume Concentration		5% Volume Concentration		Price performance ratio (€/kJ) **
		Weight of nano-particles (g)	Price of nano-PCM (€/kg)	Weight of nano-particles (g)	Price of nano-PCM (€/kg)	Weight of nano-particles (g)	Price of nano-PCM (€/kg)	
Al_2O_3	€ 0.49	44.19	€ 35.91	135.31	€ 80.56	230.26	€ 127.09	0.51
CeO_2	€ 3.62	77.02	€ 293.07	235.82	€ 867.95	401.32	€ 1,467.02	6.89
CoO	€ 0.49	81.57	€ 54.23	249.74	€ 136.63	425.00	€ 222.51	1.06
CuO	€ 0.69	82.07	€ 70.89	251.29	€ 187.65	427.63	€ 309.33	1.48
Gd_2O_3	€ 20.82	96.46	€ 2,022.65	295.36	€ 6,163.67	502.63	€ 10,479.05	53.09
Fe_2O_3	€ 0.89	66.16	€ 73.14	202.58	€ 194.55	344.74	€ 321.08	1.44
MgO	€ 0.49	45.20	€ 36.41	138.40	€ 82.08	235.53	€ 129.67	0.53
NiO	€ 0.89	80.81	€ 86.18	247.42	€ 234.47	421.05	€ 389.00	1.86
SiO_2	€ 0.49	33.46	€ 30.66	102.45	€ 64.46	174.34	€ 99.69	0.39
$SrO.TiO_3$	€ 0.45	64.52	€ 43.29	197.55	€ 103.16	336.18	€ 165.54	0.76
SnO_2	€ 0.79	70.20	€ 69.72	214.95	€ 184.07	365.79	€ 303.23	1.35
TiO_2	€ 0.59	53.66	€ 45.92	164.30	€ 111.20	279.61	€ 179.23	0.76
Y_2O_3	€ 0.59	63.13	€ 51.51	193.30	€ 128.31	328.95	€ 208.34	0.92
ZnO	€ 1.18	71.09	€ 98.14	217.65	€ 271.09	370.39	€ 451.33	2.07

***** Paraffin (RT44HC) price is 14.26 €/kg

** $\text{Price} - \text{performance ratio } (€/kJ) = \frac{\text{price of nano-PCM } (€/kg)}{\text{total enthalpy of nano-PCM } (kJ/kg)}$

4. Conclusions

This article is focused on numerical analyses of fourteen metal-oxides based nano-PCMs to establish a holistic approach for selecting nano-additives for optimal thermal enhancement. The simulated numerical model includes the impact of material thermo-physical properties, nano-particles size and volume concentration, and operating temperature while evaluating thermal performance enhancement in terms of charging and discharging rates, overall thermal enthalpy, heat transfer categorisation and respective temperature distribution, velocity response to natural convection and non-dimensional Nu, Pr and Ra numbers. Moreover, the economic evaluations of nano-PCM samples assist in identification of preferable metal-oxides candidates as thermal additives. The following conclusions are obtained from these numerical analyses:

- Inclusion of metal-oxides nano-particles significantly enhances the effective thermal conductivity and surface area for heat transfer. However, the dynamic viscosity also improves and overall enthalpy reduces. Hence, an increase in volume concentration of nano-particles increase the conductive heat transfer and curtail the buoyancy driven natural convection.
- In charging cycles, the heat transfer is mainly divided into three stages: an earlier conduction dominant period of rapidly charging nano-PCM around tube boundaries, followed by natural convection dominant upward rise of high temperature liquefied nano-PCM and final stage of weaker and gradually reducing natural convection dominant heat transfer between solid and liquefied nano-PCM at lower section of shell container. The reason behind weaker and depleting natural convection is the stratification of liquefied nano-PCM in upper section.

- In discharging cycles, heat transfer is dominated by conduction with symmetrical temperature contours in both lower and upper section of shell container. In earlier stages, a rapid formation of thin solid layers around tubes boundaries are noticed. In next stages, the thickness of solidified layers increase which results in augmented thermal resistance and consequently, the heat flux is rapidly reduced. In final stages, the continued increase in thickness of solidified layers and reduction in temperature gradient results in weakened and gradually depleting heat flux.
- Increase in volume concentration can augment peak heat flux and phase transition rate. However, the convective heat transfer coefficient and Nu are reduced due to relative increase in effective dynamic viscosity. For instance, the percentage enhancement in charging rate of SiO_2 based nano-PCM samples with 1% and 5% volume concentrations are 29.45% and 41.04%, respectively. Likewise, the discharging rates are improved by 21.09% and 30.08%, respectively.
- Metal-oxides with lower density can accommodate more nano-particles in base paraffin for given volume concentration and therefore, the specific surface area for heat transfer can be increased. In consequence, a higher phase transition rate can be achieved. For instance, SiO_2, Al_2O_3, MgO and TiO_2 based nano-PCMs demonstrate relatively higher charging/discharging rates and reasonable reduction in total enthalpy.
- Inclusion of nano-particles can significantly enhance charging/discharging rates at the cost of reduction in overall enthalpy and increase in total cost. Hence, there is trade-off between optimum thermal performance and higher cost of nano-PCM. It is identified from price-performance ratios that SiO_2, Al_2O_3, MgO and TiO_2 are preferable nano-additives due to their relatively lower cost and excellent thermal enhancement.

Acknowledgement

The authors would like to acknowledge financial support provided by Bournemouth University, UK and National University of Sciences & Technology, Pakistan (BU grant number 8399).

References

[1] REN21, Renewables 2017 Global Status Report, Paris: REN21 Secretariat, 2017.

[2] M. Höök, X. Tang, Depletion of fossil fuels and anthropogenic climate change—A review, Energy Policy, 52 (2013) 797-809.

[3] L.F. Cabeza, A. Castell, C.d. Barreneche, A. De Gracia, A. Fernández, Materials used as PCM in thermal energy storage in buildings: a review, Renewable and Sustainable Energy Reviews, 15(3) (2011) 1675-1695.

[4] Z. Khan, Z. Khan, A. Ghafoor, A review of performance enhancement of PCM based latent heat storage system within the context of materials, thermal stability and compatibility, Energy Conversion and Management, 115 (2016) 132-158.

[5] J.P. da Cunha, P. Eames, Thermal energy storage for low and medium temperature applications using phase change materials–a review, Applied Energy, 177 (2016) 227-238.

[6] N.S. Dhaidan, J. Khodadadi, Melting and convection of phase change materials in different shape containers: A review, Renewable and Sustainable Energy Reviews, 43 (2015) 449-477.

[7] M. Kibria, M. Anisur, M. Mahfuz, R. Saidur, I. Metselaar, A review on thermophysical properties of nanoparticle dispersed phase change materials, Energy Conversion and Management, 95 (2015) 69-89.

[8] J. Giro-Paloma, M. Martínez, L.F. Cabeza, A.I. Fernández, Types, methods, techniques, and applications for microencapsulated phase change materials (MPCM): a review, Renewable and Sustainable Energy Reviews, 53 (2016) 1059-1075.

[9] L. Liu, D. Su, Y. Tang, G. Fang, Thermal conductivity enhancement of phase change materials for thermal energy storage: A review, Renewable and Sustainable Energy Reviews, 62 (2016) 305-317.

[10] M.K. Rathod, J. Banerjee, Thermal performance enhancement of shell and tube Latent Heat Storage Unit using longitudinal fins, Applied thermal engineering, 75 (2015) 1084-1092.

[11] S. Lohrasbi, M. Gorji-Bandpy, D.D. Ganji, Thermal penetration depth enhancement in latent heat thermal energy storage system in the presence of heat pipe based on both charging and discharging processes, Energy Conversion and Management, 148 (2017) 646-667.

[12] A.A.R. Darzi, M. Jourabian, M. Farhadi, Melting and solidification of PCM enhanced by radial conductive fins and nanoparticles in cylindrical annulus, Energy Conversion and Management, 118 (2016) 253-263.

[13] Z. Khan, Z. Khan, K. Tabeshf, Parametric investigations to enhance thermal performance of paraffin through a novel geometrical configuration of shell and tube latent thermal storage system, Energy Conversion and Management, 127 (2016) 355-365.

[14] Z. Khan, Z.A. Khan, Experimental investigations of charging/melting cycles of paraffin in a novel shell and tube with longitudinal fins based heat storage design solution for domestic and industrial applications, Applied Energy, 206 (2017) 1158-1168.

[15] Z. Khan, Z.A. Khan, An experimental investigation of discharge/solidification cycle of paraffin in novel shell and tube with longitudinal fins based latent heat storage system, Energy Conversion and Management, 154 (2017) 157-167.

[16] Z. Khan, Z.A. Khan, Thermodynamic performance of a novel shell-and-tube heat exchanger incorporating paraffin as thermal storage solution for domestic and commercial applications, Applied Thermal Engineering, 160 (2019) 114007.

[17] J. Khodadadi, L. Fan, H. Babaei, Thermal conductivity enhancement of nanostructure-based colloidal suspensions utilized as phase change materials for thermal energy storage: a review, Renewable and Sustainable Energy Reviews, 24 (2013) 418-444.

[18] M. Xia, Y. Yuan, X. Zhao, X. Cao, Z. Tang, Cold storage condensation heat recovery system with a novel composite phase change material, Applied Energy, 175 (2016) 259-268.

[19] S. Sharshir, G. Peng, L. Wu, F. Essa, A. Kabeel, N. Yang, The effects of flake graphite nanoparticles, phase change material, and film cooling on the solar still performance, Applied energy, 191 (2017) 358-366.

[20] Z.-T. Yu, X. Fang, L.-W. Fan, X. Wang, Y.-Q. Xiao, Y. Zeng, X. Xu, Y.-C. Hu, K.-F. Cen, Increased thermal conductivity of liquid paraffin-based suspensions in the presence of carbon nano-additives of various sizes and shapes, Carbon, 53 (2013) 277-285.
[21] T. Qian, J. Li, Octadecane/C-decorated diatomite composite phase change material with enhanced thermal conductivity as aggregate for developing structural–functional integrated cement for thermal energy storage, Energy, 142 (2018) 234-249.
[22] K. Kant, A. Shukla, A. Sharma, P.H. Biwole, Heat transfer study of phase change materials with graphene nano particle for thermal energy storage, Solar Energy, 146 (2017) 453-463.
[23] Y. Yuan, N. Zhang, T. Li, X. Cao, W. Long, Thermal performance enhancement of palmitic-stearic acid by adding graphene nanoplatelets and expanded graphite for thermal energy storage: A comparative study, Energy, 97 (2016) 488-497.
[24] Y. Tang, D. Su, X. Huang, G. Alva, L. Liu, G. Fang, Synthesis and thermal properties of the MA/HDPE composites with nano-additives as form-stable PCM with improved thermal conductivity, Applied Energy, 180 (2016) 116-129.
[25] R.J. Warzoha, A.S. Fleischer, Improved heat recovery from paraffin-based phase change materials due to the presence of percolating graphene networks, International Journal of Heat and Mass Transfer, 79 (2014) 314-323.
[26] M. Alizadeh, K. Hosseinzadeh, H. Mehrzadi, D. Ganji, Investigation of LHTESS filled by Hybrid nano-enhanced PCM with Koch snowflake fractal cross section in the presence of thermal radiation, Journal of Molecular Liquids, 273 (2019) 414-424.
[27] K. Hosseinzadeh, M. Alizadeh, M. Tavakoli, D. Ganji, Investigation of phase change material solidification process in a LHTESS in the presence of fins with variable thickness and hybrid nanoparticles, Applied Thermal Engineering, 152 (2019) 706-717.
[28] Z. Khan, Z.A. Khan, Experimental and numerical investigations of nano-additives enhanced paraffin in a shell-and-tube heat exchanger: a comparative study, Applied Thermal Engineering, 143 (2018) 777–790.
[29] A.L. Owolabi, H.H. Al-Kayiem, A.T. Baheta, Nanoadditives induced enhancement of the thermal properties of paraffin-based nanocomposites for thermal energy storage, Solar Energy, 135 (2016) 644-653.
[30] S.C. Lin, H.H. Al-Kayiem, Evaluation of copper nanoparticles–Paraffin wax compositions for solar thermal energy storage, Solar Energy, 132 (2016) 267-278.
[31] M. Said, H. Hassan, Effect of using nanoparticles on the performance of thermal energy storage of phase change material coupled with air-conditioning unit, Energy Conversion and Management, 171 (2018) 903-916.
[32] S. Harikrishnan, M. Deenadhayalan, S. Kalaiselvam, Experimental investigation of solidification and melting characteristics of composite PCMs for building heating application, Energy Conversion and Management, 86 (2014) 864-872.
[33] S.I. Golestaneh, G. Karimi, A. Babapoor, F. Torabi, Thermal performance of co-electrospun fatty acid nanofiber composites in the presence of nanoparticles, Applied Energy, 212 (2018) 552-564.
[34] A. Babapoor, G. Karimi, Thermal properties measurement and heat storage analysis of paraffinnanoparticles composites phase change material: Comparison and optimization, Applied Thermal Engineering, 90 (2015) 945-951.
[35] A. Babapoor, G. Karimi, M. Khorram, Fabrication and characterization of nanofiber-nanoparticle-composites with phase change materials by electrospinning, Applied Thermal Engineering, 99 (2016) 1225-1235.
[36] S. Ebadi, S.H. Tasnim, A.A. Aliabadi, S. Mahmud, Geometry and nanoparticle loading effects on the bio-based nano-PCM filled cylindrical thermal energy storage system, Applied Thermal Engineering, 141 (2018) 724-740.
[37] S. Ebadi, S.H. Tasnim, A.A. Aliabadi, S. Mahmud, Melting of nano-PCM inside a cylindrical thermal energy storage system: Numerical study with experimental verification, Energy Conversion and Management, 166 (2018) 241-259.

[38] M. Al-Jethelah, S.H. Tasnim, S. Mahmud, A. Dutta, Nano-PCM filled energy storage system for solar-thermal applications, Renewable energy, 126 (2018) 137-155.
[39] R. Sharma, P. Ganesan, V. Tyagi, H. Metselaar, S. Sandaran, Thermal properties and heat storage analysis of palmitic acid-TiO2 composite as nano-enhanced organic phase change material (NEOPCM), Applied Thermal Engineering, 99 (2016) 1254-1262.
[40] R. Hossain, S. Mahmud, A. Dutta, I. Pop, Energy storage system based on nanoparticle-enhanced phase change material inside porous medium, International Journal of Thermal Sciences, 91 (2015) 49-58.
[41] N.S. Dhaidan, J. Khodadadi, T.A. Al-Hattab, S.M. Al-Mashat, Experimental and numerical study of constrained melting of n-octadecane with CuO nanoparticle dispersions in a horizontal cylindrical capsule subjected to a constant heat flux, International Journal of Heat and Mass Transfer, 67 (2013) 523-534.
[42] X. Zhang, X. Chen, Z. Han, W. Xu, Study on phase change interface for erythritol with nano-copper in spherical container during heat transport, International Journal of Heat and Mass Transfer, 92 (2016) 490-496.
[43] C.-J. Ho, J. Gao, An experimental study on melting heat transfer of paraffin dispersed with Al2O3 nanoparticles in a vertical enclosure, International Journal of Heat and Mass Transfer, 62 (2013) 2-8.
[44] Z. Qian, H. Shen, X. Fang, L. Fan, N. Zhao, J. Xu, Phase change materials of paraffin in h-BN porous scaffolds with enhanced thermal conductivity and form stability, Energy and Buildings, 158 (2018) 1184-1188.
[45] W. Yuan, X. Yang, G. Zhang, X. Li, A thermal conductive composite phase change material with enhanced volume resistivity by introducing silicon carbide for battery thermal management, Applied Thermal Engineering, 144 (2018) 551-557.
[46] P. Bose, V.A. Amirtham, A review on thermal conductivity enhancement of paraffinwax as latent heat energy storage material, Renewable and Sustainable Energy Reviews, 65 (2016) 81-100.
[47] H. Helvaci, Z.A. Khan, Heat transfer and entropy generation analysis of HFE 7000 based nanorefrigerants, International Journal of Heat and Mass Transfer, 104 (2017) 318-327.
[48] Rubitherm® Technologies GmbH, http://www.rubitherm.eu/en/, in, 2018.
[49] Sigma-Aldrich Company Ltd., https://www.sigmaaldrich.com/united-kingdom.html, in, 2018.
[50] Iolitec Ionic Liquids Technologies GmbH, https://iolitec.de/en, in, 2018.
[51] M. Parsazadeh, X. Duan, Numerical and statistical study on melting of nanoparticle enhanced phase change material in a shell-and-tube thermal energy storage system, Applied Thermal Engineering, 111 (2017) 950-960.
[52] J.M. Mahdi, S. Lohrasbi, D.D. Ganji, E.C. Nsofor, Accelerated melting of PCM in energy storage systems via novel configuration of fins in the triplex-tube heat exchanger, International Journal of Heat and Mass Transfer, 124 (2018) 663-676.
[53] O. Mahian, L. Kolsi, M. Amani, P. Estellé, G. Ahmadi, C. Kleinstreuer, J.S. Marshall, M. Siavashi, R.A. Taylor, H. Niazmand, Recent advances in modeling and simulation of nanofluid flows-part I: fundamental and theory, Physics reports, (2018).
[54] D.D. Gray, A. Giorgini, The validity of the Boussinesq approximation for liquids and gases, International Journal of Heat and Mass Transfer, 19(5) (1976) 545-551.
[55] D.A. Nield, A. Bejan, Nield-Bejan... Convection in porous media, Springer, 2006.
[56] M.T. Chaichan, H.A. Kazem, Single slope solar distillator productivity improvement using phase change material and Al 2 O 3 nanoparticle, Solar Energy, 164 (2018) 370-381.
[57] K. Venkitaraj, S. Suresh, B. Praveen, A. Venugopal, S.C. Nair, Pentaerythritol with alumina nano additives for thermal energy storage applications, Journal of Energy Storage, 13 (2017) 359-377.
[58] M. Corcione, Empirical correlating equations for predicting the effective thermal conductivity and dynamic viscosity of nanofluids, Energy Conversion and Management, 52(1) (2011) 789-793.
[59] R. Kandasamy, X.-Q. Wang, A.S. Mujumdar, Transient cooling of electronics using phase change material (PCM)-based heat sinks, Applied Thermal Engineering, 28(8-9) (2008) 1047-1057.

[60] R.S. Vajjha, D.K. Das, Experimental determination of thermal conductivity of three nanofluids and development of new correlations, International Journal of Heat and Mass Transfer, 52(21-22) (2009) 4675-4682.
[61] J.C. Maxwell, A treatise on electricity and magnetism, Oxford: Clarendon Press, 1873.
[62] V.D. Bruggeman, Berechnung verschiedener physikalischer Konstanten von heterogenen Substanzen. I. Dielektrizitätskonstanten und Leitfähigkeiten der Mischkörper aus isotropen Substanzen, Annalen der physik, 416(7) (1935) 636-664.
[63] R.L. Hamilton, O. Crosser, Thermal conductivity of heterogeneous two-component systems, Industrial & Engineering chemistry fundamentals, 1(3) (1962) 187-191.
[64] Y. Xuan, Q. Li, W. Hu, Aggregation structure and thermal conductivity of nanofluids, AIChE Journal, 49(4) (2003) 1038-1043.
[65] O. Mahian, L. Kolsi, M. Amani, P. Estellé, G. Ahmadi, C. Kleinstreuer, J.S. Marshall, R.A. Taylor, E. Abu-Nada, S. Rashidi, Recent advances in modeling and simulation of nanofluid flows-part II: applications, Physics reports, (2018).
[66] V.T. Morgan, The overall convective heat transfer from smooth circular cylinders, in: Advances in heat transfer, Elsevier, 1975, pp. 199-264.